Adaptive mesh axi-symmetric simulation of droplet impact with a spherical particle in mid-air

Ikroh Yoon, Jalel Chergui, Damir Juric, Seungwon Shin

Adaptive mesh axi-symmetric simulation of droplet impact with a spherical particle in mid-air

Ikroh Yoon[1], Jalel Chergui[2], Damir Juric[2,3] and Seungwon Shin[4,a]

[1]Korea Institute of Marine Science and Technology Promotion (KIMST), Seoul, 06775 Korea, iryoon@kimst.re.kr

[2]Centre National de la Recherche Scientifique (CNRS), Laboratoire Interdisciplinaire des Sciences du Numérique (LISN), Université Paris Saclay, 91400 Orsay, France, Damir.Juric@limsi.fr, Jalel.Chergui@limsi.fr

[3]Department of Applied Mathematics and Theoretical Physics, University of Cambridge, Centre for Mathematical Sciences, Wilberforce Road, Cambridge CB3 0WA, UK

[4]Department of Mechanical and System Design Engineering, Hongik University, Seoul, 04066 Korea, sshin@hongik.ac.kr

[a)] Corresponding Author:
Professor Seungwon Shin, PhD
Phone: 82-2-320-3038
FAX: 82-2-322-7003
E-Mail: sshin@hongik.ac.kr

ABSTRACT

In this study, droplet-particle collisions in mid-air are numerically investigated for a wide range of collision parameters: Weber number, contact angle and droplet/particle diameter ratio ($4 \leq We \leq 150$, $20° \leq \theta_{eqi} \leq 160°$, and $\Omega = 1/2$ and 1). To perform these simulations in an efficient manner, a simple dual grid based adaptive mesh refinement (SDG AMR) strategy is proposed and implemented in our existing multiphase flow solver. A total of 90 collision cases are systematically analyzed and are compared with results for the case of impact on a stationary particle to understand how mid-air collision characteristics are changed relative to those on a stationary target. The simulation results show that mid-air droplet-particle collision behavior is significantly different from that of droplet collision on a stationary particle, thus the impact phenomena cannot be interpreted by extrapolating collision results for a stationary target.

Keywords: droplet impact; spherical particle; mid-air collision; multiphase flow; numerical simulation

I. INTRODUCTION

Liquid droplet collision with a solid particle in mid-air is commonly observed in nature. For example, small air-borne particles are often removed from the atmosphere by raindrops in a natural scrubbing process (Mitra et al., 2017) while, on the other hand, atmospheric aerosol particles also play a role as cloud condensation nuclei (Hoose et al., 2008). The role of ocean spray, bubbles and droplets created at the air/sea interface, can have a large influence on weather and climate. Small droplets of sea-salt aerosols can be carried high into the atmosphere to interact with air-borne particles to seed clouds and affect the amount of sunlight absorbed or reflected and additionally contribute to ocean-atmosphere heat exchange through latent heat of evaporation.

These collision phenomena can also be widely found in many engineering applications across diverse processes from fluid catalytic cracking (FCC) in petrochemical industries (Teunou and Poncelet, 2002) to tablet coating in pharmaceutical industries (Bolleddula *et al*., 2010). A representative example is spray drying which is widely used as an encapsulation process in the chemical, pharmaceutical and food industries (Nedovic *et al*., 2011). This process is one of the most essential unit operations for producing powder using liquid slurry (Khojasteh *et al*., 2016) in which the collision behavior between droplets and particles significantly affects the product quality such as the morphology of the powder or release characteristics of an active substance in a micro-encapsulated core (Hoeven, 2008).

Despite its importance, few studies have focused on droplet collision with a particle, especially in mid-air, and a majority of the recent studies in the literature have been devoted to impact phenomena with a flat surface. (See the recent reviews by Yarin (2006), Josserand and Thoroddsen (2016) and references therein.) Only recently has droplet collision on a curved surface begun to receive attention. Hardalupas *et al.* (1999) investigated splashing criteria and

the effect of target curvature on the onset of splashing. They experimentally showed that splashing was promoted at smaller particle scales. Rozhkov *et al*. (2002, 2003) showed that a droplet colliding onto a small disk presents significantly different behavior compared to collision on a flat surface in terms of the motion of thin liquid lamellae. Bakshi *et al*. (2007) theoretically and experimentally studied the characteristics of liquid film thickness and showed that the non-dimensional film thickness profiles collapsed onto a single curve in the initial-drop-deformation phase and inertia-dominated phase during impact on a spherical particle. Ge and Fan (2007) studied droplet-particle collision in the film boiling regime and analyzed the effect of particle size on both the maximum spreading and the contact time of the droplet. Malgarinos *et al*. (2016) numerically investigated droplet-particle collision using three-dimensional Volume-of-Fluid simulations. They identified the boundary separating coating outcomes from rebound and the film thickness as well as wetting area were also quantified. Zhu *et al*. (2017) investigated the film thickness and showed that the thickness of liquid film can be described well by scaling laws at moderate Weber (We) and Reynold number (Re). Mitra *et al*. (2013a, 2016, 2017) experimentally studied the collision system with varying droplet-to-particle size ratio and performed very extensive analysis to characterize the impact behavior. Although significant knowledge gaps have been covered by their studies, the analysis focused mainly on heat transfer characteristics during the collision. Banitabaei and Amirfazli (2017) addressed droplet-particle collision for a very wide range of We (0.1-1145) and quantitatively analyzed the lamella structure and its dynamics. Liu *et al*. (2019) carried out theoretical, numerical, and experimental investigations of droplet-particle collision and quantified the effect of particle size on the maximum spreading of the droplet. Khurana *et al*. (2019) also experimentally and theoretically studied the post-impact phenomena of droplet impact onto a spherical particle and proposed an analytical model to predict the maximum spread angle of the droplet on a particle. Recently, Yoon and Shin (2021a, 2021b) presented 7

collision outcomes with outcome regime maps (Yoon and Shin, 2021b) and analyzed the dynamic characteristics of the droplet-particle interaction system (Yoon and Shin, 2021a). They further analyzed the maximal spreading of droplet-particle collision for a wide range of Ohnesorge number ($0.0013 \leq Oh \leq 0.7869$) and also proposed an empirical model which can be applied to droplet impact with both a flat surface and a particle (Yoon and Shin, 2021c). While these studies have provided greatly useful knowledge for understanding physical phenomena related to the droplet-particle collision system, the major findings have been focused on collisions with a stationary particle, not on collisions in mid-air.

For the case of mid-air droplet-particle collision Dubrovsky *et al*. (1992) investigated droplet collision with both a stationary and in-flight particle and analyzed the mass transfer characteristics between droplet and particle. Mitra *et al*. (2013b) considered the droplet impact with a falling particle and quantitatively investigated the mass of attached droplet on the particle. He *et al*. (2013) experimentally studied the collisions between free-falling solid particles and liquid spray droplets but their results focused on the statistical distribution of liquid attachment and collision probability rather than understanding the physical behavior of collision phenomena. Gac and Gradon (2014) performed Lattice–Boltzmann simulations for a small We range (0.63–1.3) but the result was limited to providing qualitative analysis without detailed quantification and validation. Sechenyh and Amirfazli (2016) extensively studied the impact outcomes and outcome transition boundaries for a relatively high Weber number range ($We \leq 2500$). They also quantitatively analyzed the structure of stretched liquid lamellae during the collision. Pawar *et al*. (2016) also experimentally studied the collision behavior of a droplet with a particle and presented an impact outcome regime map. They considered a particle as a stationary target before the collision but allowed the particle to freely move after the collision. Malgarinos *et al*. (2017a, 2017b) performed two- and three-dimensional Volume-of-Fluid simulations of droplet-particle interaction at high temperature conditions ($T \geq 800$ K).

More complicated phenomena, e.g., phase change and surface reactions were also considered in their numerical studies. Yang and Chen (2018) investigated the collision system between a freely moving droplet and a freely moving particle using a Lattice–Boltzmann method. They considered three different surface wettability characteristics but their results were limited to two-dimensional simulations (cylindrical objects). Recently, Banitabaei and Amirfazli (2020) performed an extensive analysis of droplet-particle collisions in mid-air. They examined the effect of diameter ratio, liquid viscosity, and ambient gas density on the collision phenomena, especially in terms of the stretched lamellae characteristics.

Despite the various studies heretofore undertaken it still remains difficult to understand the underlying physics that dominates the collision process. For a collision in mid-air, the momentum exchange between droplet and particle is complicated by the coupling of contact angle dynamics and droplet spreading. It is natural to expect that the spreading momentum would be reduced compared to collision with a stationary target. Therefore, a fundamental question can be raised: Can droplet-particle collision in mid-air be simply interpreted by extrapolating the (relatively well-known) collision phenomena on a stationary target with an appropriate re-scaled parameter (such as reduced impact Weber number)? A systematic approach considering the variations of various controlling variables as well as comparisons with the corresponding stationary target cases would help in understanding the overall phenomena involved in mid-air droplet-particle interaction. To the best of our knowledge, however, no clear answer to this question has been addressed and any detailed systematic comparison between the two systems (i.e. collision in mid-air and collision with a stationary particle) has not yet been presented.

Experimental research on mid-air droplet-particle collisions has provided valuable data but suffers from difficulties in precise control of experimental conditions (Mitra *et al*., 2017) due to the limited length and/or time scales available to the measurement techniques. For

example, to achieve a sufficiently precise and well-controlled head-on collision in mid-air, at least ten trials or more were needed even in the recent well-controlled experiment of Banitabaei and Amirfazli (2020). On the other hand, numerical simulations can provide a useful complementary approach in investigating mid-air droplet-particle collision. The small length and/or time scales related to droplet-particle interactions of interest can usually but not always be well resolved. Numerical approaches can also provide the detailed flow field inside the droplet as well as the evolution of the liquid-gas phase interface. The collision conditions, which are generally difficult to control precisely in experimental work, can also be easily controlled.

However, numerical simulations are themselves limited by practical considerations such as the computational resources and computing time necessary when the range of time and especially length scales are very large. A large computational domain is required to observe the entire collision process in a systematic investigation of mid-air droplet-particle interaction for a wide range of input conditions. A droplet colliding on a solid target can exhibit greatly deformed lamellae, to dimensions larger than several times the initial droplet diameter (Banitabaei and Amirfazli, 2017; Khurana *et al*., 2019; Liu *et al*., 2019; Yoon and Shin, 2021b, 2021c). In the case of droplet collision with a stationary particle, quite large computational domains, i.e. 5-25 times the initial droplet diameter, are generally used to capture the physical phenomena and minimize the influence from the domain boundary (Malgarinos *et al*., 2016; Banitabaei, and Amirfazli, 2017; Yoon and Shin, 2021b). If the particle can freely move as well, then much larger simulation domains might be considered. When a droplet having a diameter of D_d collides with a particle with an impact velocity V_{ini}, the required non-dimensional time ($\tau = tV_{ini} / D_d$) to clearly capture the impact outcomes (e.g., deposition, rebound, etc.) can reach $\tau \sim$10-20 for certain cases (Yoon and Shin, 2021b). If the droplet moves and interacts with the collided particle at the velocity of V_{ini}, their travel distance can reach

nearly 20 times D_d which implies an additional increase of the computational domain size compared with the stationary case. Considering that typical numerical solutions achieve grid convergence at resolutions of 60 - 80 CPR (cells per droplet radius) (Šikalo *et al*., 2005; Malgarinos *et al*., 2016; Banitabaei and Amirfazli, 2017; Yoon and Shin, 2021b), a grid resolution on the order of 10^5 ********10^5 what? grid cells???*****might be required to sufficiently cover the size of the computational domain necessary to capture droplet deformation as well as particle movement, even for a two-dimensional simulation. Furthermore, owing to the complicated and dynamic behavior during droplet collision [for example, the local Weber number can rapidly increase to over ten times that of the initial impact We during the droplet recoil phase of the collision (Yoon and Shin, 2021a)] a very small time-step size is generally necessary. Such levels of high grid resolution and small time-step size may be acceptable for a single test case but can become a serious burden for a systematic analysis which should include a large number of simulations under various input conditions. Therefore, overcoming the constraint of limited computational resources is essential to performing a systematic analysis of the mid-air droplet-particle collision phenomena.

One of the popular strategies for reducing the computational cost is to employ an adaptive mesh refinement (AMR) technique, which generally incorporates regions of varying grid resolution within the overall computational domain (Berger and Colella, 1989; Popinet, 2003; Sussman *et al*., 1999). While well-known methods for the simulation of multiphase flows such as Volume-of-Fluid, Level-Set, and Front-Tracking have adopted a variety of appropriate AMR techniques (Agresar *et al*., 1998; Popinet, 2003), an AMR technique for our simulation framework has not yet been developed, even though our work has previously been widely applied to various droplet collision phenomena (Choi and Shin, 2019; Han *et al*., 2020; Shin *et al*., 2017; Yoon and Shin, 2021a, 2021b, 2021c) and successfully parallelized (Shin *et al*., 2017). Therefore, one of our objectives here is the development of a novel and simple AMR technique

which can be easily implemented, without major modification to our existing framework, and which can provide a useful instrument to efficiently investigate the mid-air droplet-particle collision system.

In the present study, we first propose a simple but very useful adaptive mesh refinement (AMR) strategy to perform efficient numerical simulations of the droplet-particle collision system in mid-air, and then apply this method to undertake the large number of collision cases in our systematic study. Since our aim is to understand the difference in physical characteristics between two systems (i.e. collision with a particle in mid-air and collision with a stationary particle) outcome regime maps are presented and compared for a wide range of collision conditions. The underlying mechanisms leading to different impact outcomes are also analyzed. The remainder of this paper is organized as follows: Section II explains the numerical formulation used herein. Details of the numerical method for tracking the phase interface, fluid-structure interaction (FSI) and the proposed AMR approach are described. Section III verifies the performance and efficiency of the AMR technique and analyzes the impact phenomena of mid-air droplet-particle collision. We then summarize the major findings in Section IV.

II. NUMERICAL METHOD

Here, we briefly describe the numerical methods used for droplet-particle interaction in mid-air. Since the present study focuses on the development of the AMR technique and aims at understanding the underlying physical phenomena of a droplet interacting with a moving particle, our existing numerical procedure is kept predominantly intact. The AMR serves specifically to increase computational efficiency by providing high grid resolution only where needed. Readers can find more detailed information about our existing numerical framework in our previous studies; Shin and Juric (2002, 2009), Shin *et al*. (2005, 2018), Yoon and Shin (2021b, 2021c). It is also worthwhile mentioning that these numerical methods considered here have been rigorously validated with many existing experimental studies for a wide range of collision conditions (Choi and Shin, 2019; Yoon and Shin, 2021a, 2021b, 2021c) and have also been applied to diverse studies of droplet collision phenomena which include collision with a stationary particle (Yoon and Shin, 2021a, 2021b, 2021c), a moving particle (Choi and Shin, 2019), a cylindrical wire (Han *et al*., 2020), a flat surface (Shin *et al*., 2018) and a liquid pool (Shin *et al*., 2017).

A. Governing equations

Using a single-field formulation, the governing equations for incompressible flow apply to all three phases (liquid, solid, and gas) and are solved on a fixed Cartesian (Eulerian) grid:

$$\nabla \cdot \mathbf{u} = 0 \tag{1}$$

$$\rho\left[\frac{\partial \mathbf{u}}{\partial t}+\mathbf{u}\cdot\nabla\mathbf{u}\right]=-\nabla P+\rho\mathbf{g}+\nabla\cdot\mu\left(\nabla\mathbf{u}+\nabla\mathbf{u}^{\mathrm{T}}\right)+\mathbf{F} \tag{2}$$

Here, **u** is the velocity vector, P is the pressure and **g** is the gravitational acceleration.

In the single field formulation, each phase (i.e. solid, liquid or gas) can be identified by a combination of two indicator function fields, I_{f} and I_{s}, which have characteristics of the Heaviside function and vary from zero in one phase to unity in the other phase. I_{f} and I_{s} are in turn determined from two distance functions ϕ_{f} and ϕ_{s}, which are fields defined as the distance from the fluid-fluid (liquid-gas) interface and solid-fluid interface, respectively. ****need equation defining I in terms of phi*****

Thus, the density, ρ, and the viscosity, μ, in Eq. 2 can be defined using the indicator functions I_{f} and I_{s} :

$$\rho=\left\{\rho_{\mathrm{d}}+\left(\rho_{\mathrm{a}}-\rho_{\mathrm{d}}\right)I_{\mathrm{f}}\right\}I_{\mathrm{s}}+\rho_{\mathrm{p}}\left(1-I_{\mathrm{s}}\right) \tag{3}$$

$$\mu=\left\{\mu_{\mathrm{d}}+\left(\mu_{\mathrm{a}}-\mu_{\mathrm{d}}\right)I_{\mathrm{f}}\right\}I_{\mathrm{s}}+\mu_{\mathrm{p}}\left(1-I_{\mathrm{s}}\right) \tag{4}$$

where the subscripts “d”, “a”, “p”, “f”, and “s” stand for droplet (liquid), air (gas), and particle (solid), fluid-fluid interface, and solid-fluid interface, respectively.

Another feature of the single-field formulation is that the surface tension force, **F,** in Eq. (2) is considered non-zero only at the liquid-gas interface and is described by the hybrid formulation as follows:

$$\mathbf{F}=\sigma\kappa_{\mathrm{H}}\nabla I \tag{5}$$

where σ and κ_H are the surface tension coefficient (assumed constant) and the curvature field, respectively. κ_H can be calculated as follows:

******need to remove sigma in eqs 6 and 7 ******

$$\kappa_H = \frac{\mathbf{F}_L \cdot \mathbf{G}}{\sigma \mathbf{G} \cdot \mathbf{G}} \tag{6}$$

$$\mathbf{F}_L = \int_{\Gamma(t)} \sigma \kappa_f \mathbf{n}_f \delta\left(\mathbf{x} - \mathbf{x}_f\right) \mathrm{d}s \tag{7}$$

$$\mathbf{G} = \int_{\Gamma(t)} \mathbf{n}_f \delta\left(\mathbf{x} - \mathbf{x}_f\right) \mathrm{d}s \tag{8}$$

where $\mathbf{x}_f$ is the position vector of the (fluid-fluid) Lagrangian phase interface, $\Gamma(t)$, and the surface integrals are evaluated over area (or line in 2D) element ds. κ_f is the curvature directly calculated on the Lagrangian interface. $\mathbf{n}_f$ is the unit normal vector from the interface. $\delta(\mathbf{x}\text{-}\mathbf{x}_f)$ is the Dirac delta distribution and has a value of non-zero only at the interface ($\mathbf{x} = \mathbf{x}_f$).

The Lagrangian interface is advected by temporally integrating:

$$\frac{d\mathbf{x}_f}{dt} = \mathbf{u}_f \tag{9}$$

where $\mathbf{u}_f$ is the velocity vector of the phase interface and is obtained by interpolation of the velocity vector field $\mathbf{u}$.

However, if an element is in contact with a solid particle surface (i.e. on a triple contact line), $\mathbf{x}_f$ is advected according to the Navier-slip boundary condition to avoid a stress singularity. In this case, the contact line velocity (U_{CL}) on the solid particle surface is:

$$U_{CL} = \lambda \left\{ \frac{\partial \mathbf{u}}{\partial \mathbf{n}} \right\}_{wall} \tag{10}$$

where λ is the proportionality slip constant and $\partial\mathbf{u}/\partial\mathbf{n}$ is the shear strain rate at the particle surface. In numerical practice, good representation of the hysteresis curve for dynamic contact angles (i.e. advancing and receding contact angles) is achieved for λ equal to one-quarter the size of a grid cell (Shin *et al*., 2018).

The dynamic contact angle (θ_{dyn}) is important for accurately simulating droplet collision with a solid surface (Antonini *et al*., 2012; Šikalo *et al*., 2005). In the present study, θ_{dyn} is modeled as in Yokoi *et al.* (2009):

$$\theta_{dyn}\left(U_{CL}\right) = \begin{cases} \min\left[\theta_{eqi} + \left(\dfrac{\mathrm{Ca}}{q_1} \right)^{1/3},\ \theta_{mda} \right], & \text{if } U_{CL} \geq 0 \ \text{ (for spreading)} \\ \max\left[\theta_{eqi} + \left(\dfrac{\mathrm{Ca}}{q_2} \right)^{1/3},\ \theta_{mdr} \right], & \text{if } U_{CL} \leq 0 \ \text{ (for receding).} \end{cases} \tag{11}$$

where Ca is the capillary number ($\mathrm{Ca} = \mu U_{CL}/\sigma$) and θ_{eqi} is the equilibrium contact angle. θ_{mda} and θ_{mdr} are the allowable maximum (advancing) and minimum (receding) dynamic contact angles, respectively. Contact angle hysteresis is thus represented by the difference between θ_{mda} and θ_{mdr}. We use the values in Yokoi *et al.* (2009) ($q_1 = 9.0 \times 10^{-9}$ and $q_2 = 9.0 \times 10^{-8}$) for the two experimentally determined constants q_1 and q_2 associated with the surface characteristics.

B. Level contour reconstruction method and fictitious domain method

One of the essential aspects of multiphase flow simulation is the need to accurately calculate the motion of the phase interface. In the current study, the Level Contour Reconstruction method (LCRM) was used for tracking the fluid-fluid interface. The LCRM (Shin and Juric, 2002) is a hybridization of two well-known interface methods. The LCRM takes advantage of both the Front-Tracking (Unverdi and Tryggvason, 1992; Tryggvason *et al*., 2001) and the Level-Set method (Osher and Sethian, 1988). A key point of the LCRM is that the phase interface can be represented by a moving Lagrangian mesh of interface elements (lines in 2D and triangles in 3D) for accurate tracking of the interface (as in the original Front-Tracking method), but each Lagrangian mesh element is reconstructed using the distance function ϕ_f. The distance function is a central feature of the Level-Set method, to avoid difficulties in handling topology change and the complex connectivity of elements (which is the major drawback of the original Front-Tracking method). In the LCRM, the interface elements are not logically connected, but are implicitly connected due to sharing identical edge points after reconstruction at cell faces of the underlying Cartesian (Eulerian) finite-difference grid. Hence, the difficulties in the treatment of element connectivity during topology change for example (e.g., interface merging, pinch-off and deformation) can be avoided while maintaining the advantages of the original Front-tracking method particularly the accurate representation of the phase interface and capillary forces using the Lagrangian grid.

Fig.1 shows the basic concept of the interface reconstruction in the LCRM. As described above, the phase interface is represented and is tracked using Lagrangian mesh elements (red lines), but can also be represented simultaneously by a specific contour of the distance function (ϕ_f) field on the Cartesian (Eulerian) grid (green mesh on the left side of Fig.1). Since ϕ_f has a

value of zero at the interface, the Lagrangian interface elements can be regenerated by connecting two points where $\phi_f = 0$ at the cell boundaries of the Cartesian grid (blue grid on the right side of Fig.1). The precise locations for these reconstruction points are accurately obtained using an appropriate high-order interpolation scheme. Because the reconstruction is performed at the cell boundaries, every interface element is naturally linked (due to end points of neighboring elements sharing the same location) after reconstruction. More detailed information about the LCRM can be found in Shin and Juric (2002; 2009) and Yoon and Shin (2021b).

To track the solid-fluid interface (the moving solid particle), we use the fictitious domain method (FDM) (Glowinski *et al*., 1999; Mirzaii and Passandideh-Fard, 2012) for the fluid-structure interaction (FSI) modeling which assumes a moving solid as one of the phases but with a fictional large viscosity. Thus, the Navier-Stokes equations are applied to the entire flow field including the solid region. The FDM enables a solid region of arbitrarily complex shape to be easily represented in the (Cartesian) Eulerian grid without needing a boundary fitted unstructured mesh. Therefore, the FDM can be easily extended to the existing LCRM framework in which the governing equations are already solved as a single-field formulation on the fixed Eulerian grid.

The solid region for a spherical particle is simply identified by using the distance function ϕ_s which can be generated analytically for a circle (2D) or sphere (3D). The interface deformation is negligible for the solid-fluid interface since the particle can be assumed to be a rigid body. Rotation of the particle can also be neglected because we only consider here an axi-symmetric head-on collision. Therefore, the dynamics of the particle can be completely represented by the motion of the paricle centroid, $\mathbf{x}_s$. The solid motion is directly forced by applying the averaged translational velocity as follows:

$$\mathbf{u}_s = \frac{\int_s \rho_p \mathbf{u} d\forall}{M} \tag{12}$$

where $\mathbf{u}_s$ is the averaged velocity vector of the particle and M and ρ_p are the mass and the density of the particle, respectively. The velocity field inside the solid region is replaced by this momentum averaged velocity to describe its rigid body motion. The motion of the particle is calculated by integrating its centroid position $\mathbf{x}_s$ over time:

$$\frac{d\mathbf{x}_s}{dt} = \mathbf{u}_s \tag{13}$$

Similar to the Lagrangian element advection in Eq. (9), the centroid position of the particle is integrated with a 2nd order Runge-Kutta method. We found that setting the viscosity of the solid to be 100 times that of the liquid is sufficient to represent the solid particle dynamics (Choi and Shin, 2019; Mirzaii and Passandideh-Fard, 2012). This treatment can be extended to more complex shaped solids by including rotational components. Several benchmark tests for the moving solid were performed in a previous paper and showed good accuracy compared with experimental data (Choi and Shin, 2019).

C. Simple dual grid based adaptive mesh refinement strategy

We introduce here a simple dual grid based adaptive mesh refinement (SDG AMR) technique. As mentioned before, an AMR strategy for mid-air droplet-particle simulations is essential for computing efficiency with limited computational resources. Although our computational framework based on the LCRM has been extensively applied to various simulations of multiphase flow problems (Choi and Shin, 2019; Han *et al.*, 2020; Shin *et al.*,

2017; Yoon and Shin, 2021a; 2021b) and even was successfully parallelized for high-performance computational resources (Shin *et al*., 2017) in fully three-dimensional problems, an AMR technique has not yet been applied for this framework.

AMR techniques dynamically and automatically adjust the grid configuration in a numerical simulation to reduce the computational cost while maintaining required accuracy (Berger and Colella, 1989; Popinet, 2003) and can be generally categorized into two categories depending on the grid configuration approach: patch-based AMR (Berger and Colella, 1989; Griffith *et al*., 2007; Roma *et al*., 1999) and tree-based AMR (Fakhari and Lee, 2014; Popinet, 2003; Zuzio and Estivalezes, 2011). These two categories are similar in the sense that the different grid resolutions are simultaneously applied to a single system. On the other hand, the detailed method for these grid configurations as well as the data structures needed considerably differ from each other. Patch-based AMR, originally developed by Berger and Colella (1989), generally uses multiple rectangular patches with different grid resolution. The patches with different grid resolutions are linked through the boundaries. Since the patches are usually rectangular, the boundaries of patches are aligned with the Cartesian grid. Array- and cache-based data structures can also be used since the size of the grid in each patch is generally a constant value. Conversely, tree-based AMR recursively bisects the grid cells where a finer grid resolution is required (Popinet, 2003). Since a single cell (the cell before bisection is generally referred to as the root cell) can be selectively bisected generating 4 (for a two-dimensional domain) or 8 (for a three-dimensional domain) leaf cells, various grid resolutions can be densely applied to certain local regions of interest. In terms of efficient deployment of refined cells, tree-based AMR approaches can generally provide a more localized and optimized grid configuration compared to patch-based AMR.

In implementing AMR into a working computational framework, it is important to consider not only the pros and cons of the candidate strategies but also the practical issue of

developing an efficient yet modular AMR technique adapted for an existing code framework. The two types of AMR mentioned above (i.e. patch- and tree-based techniques) have been successfully applied to both the Front-Tracking and Level-Set method contexts (Agresar *et al*., 1998; Pivello *et al*., 2014; Sussman *et al*., 1999; Zuzio and Estivalezes, 2011) which form the basis of the LCRM. Thus, they could both be good candidates for our existing (LCRM-based) computational framework. In this current work, the two main aspects we considered are: (1) the ease of implementation in our existing LCRM-based procedure and (2) possible scalability for future extensions to a parallelized three-dimensional version. For a tree-based AMR strategy, extensive changes in the existing data structure as well as in the solution process were seen to be required. In the type of simulation we study here, droplet-particle interaction, the region of most interest is confined near the fluid-fluid and fluid-solid interface. Away from those interfaces, velocity fields are usually very small and smoothly decay toward the physical boundary. Relatively low resolution would be sufficient for this outer region. Thus, we prefer, the patch-based AMR approach as a more suitable choice in representing these two distinct regions requiring different mesh resolutions.

Here we describe an implementation of patched-based AMR in which the detailed techniques for the grid configuration and related algorithms are quite different from the conventional patch-based approach. Fig. 2(a) depicts the basic concept of this Simple-Dual-Grid Adaptive Mesh Refinement (SDG AMR) method proposed here. The (deformable and moving) fluid-fluid phase interface is represented by Lagrangian mesh elements (black lines sharing red dots) and the governing equations are solved on the fixed (Cartesian) Eulerian grid (white Eulerian domain). In our original framework without AMR, any necessary information was exchanged between these two grid systems only (Lagrangian and fixed Eulerian grids) (Shin and Juric, 2002). Now we apply an additional Eulerian (rectangular) domain with a higher grid resolution over the region requiring higher accuracy (i.e. region near the droplet

and particle interfaces in the current study). The underlying under-resolved (white) Eulerian domain still covers the entire physical domain including the outer region requiring less resolution. These two Eulerian grid layers, i.e. the High-Resolution Grid (orange domain surrounded by thick green lines) and the Low-Resolution Grid (white domain) are referred to as HRG and LRG hereafter, respectively.

Although the HRG and LRG layers have different grid resolutions, the same governing equations are applied to each layer. The boundary conditions at the HRG layer are obtained by interpolating values from the LRG layer [see gray cells and red dashed arrow lines in Fig. 2(a)]. For selecting an appropriate interpolation scheme, we have considered several techniques which have been used in the literature from first-order linear (Berger and Colella, 1989; Popinet, 2003) to fourth-order interpolation (Sussman *et al*., 1999; Zuzio and Estivalezes, 2011). After extensive preliminary tests, we found that the solution retains sufficient accuracy with a third-order interpolation scheme if the flow is smooth near the phase interface (Roma *et al*., 1999). Here we choose cubic spline interpolation.

Due to the Front Tracking aspects of the LCRM, information exchange between the Lagrangian grid (the phase interface) and the Eulerian grid layers is necessary for the calculation of the interface curvature as well as physical property fields (from the Lagrangian to the Eulerian grid) or the advection of interfacial elements (from the Eulerian to the Lagrangian). Thus, the three grid systems are closely coupled (see blue and red dashed arrow lines). As can be seen in the figure, the flow field obtained at the HRG layer is used to update the position of the interface elements (from the HRG to the Lagrangian grid). Interface reconstruction is also performed at the HRG layer. Interfacial forces are evaluated both on the HRG and LRG (from the Lagrangian to the two different Eulerian grids). Note that the governing equations then are solved twice on the different grid layers. Note that the solutions on the HRG and LRG can now proceed separately. This flexibility is the key difference

compared to the conventional patch-based AMR which does not retain and compute the LRG portion of the domain that overlaps with the HRG layer. Since the LRG layer has relatively low resolution, the sacrifice of additional computation in this portion of the LRG is practically acceptable since this allows a common solver (Navier-Stokes module) to be applied to each layer without modification (see the blue box in Fig.2(a)). We provide a more detailed description of the overlapping patch approach below.

Within our SDG AMR framework, the position and size of the HRG layer can be changed during the calculation depending on the motion of the droplet and solid particle. These is accomplished by a re-grid procedure of the HRG layer. Fig. 2(b) depicts the basic concept of translation and expansion (or contraction) of the HRG layer. The HRG layer can simply be moved, keeping its size, or can extend (or reduce) its size as needed for the problem at hand. This re-grid process for the HRG layer should be clearly distinguished from the reconstruction of the Lagrangian moving mesh in the LCRM procedure. Note that the grid resolution (i.e. size of the grid cell) of the HRG layer is not changed after the re-grid procedure. New HRG cells are added for expansion or existing HRG cells are deleted for contraction. Therefore, the total number of HRG cells could increase (or decrease) depending on the expansion (or contraction) of the HRG layer but the grid cell size in the HRG is not changed. Since the boundaries of HRG layer (see green thick lines in Fig.2), which we will call the fine/coarse boundary, is always aligned with the grid lines of the LRG layer even after the re-grid, thus no modification of the numerical solver is necessary due to this re-grid procedure.

As can be seen in Fig. 2(b), the fine/coarse boundary is chosen to surround the objects of interest (i.e. the droplet and particle) that need to be simulated with a finer grid. Since the phase interfaces are represented by the Lagrangian grid (fluid-fluid interface) or by the distance function ϕ_s (fluid-solid interface) in our numerical formulation, identifying the maximum (or minimum) locations of interfaces in the Cartesian coordinate system is straightforward.

Therefore, choosing the position of the fine/coarse boundary is straightforward and includes a pre-determined clearance distance (L_i). Note that any complicated algorithms such as tagging and related computations (Berger and Colella, 1989; Fakhari and Lee, 2014; Griffith *et al*., 2007; Popinet, 2003; Roma *et al*., 1999) are not required to determine the fine/coarse boundary. The HRG layer is needed only near the phase interface and neighboring area at which physical properties vary significantly (Fakhari and Lee, 2014; Roma *et al*., 1999).

As the phase interfaces are advected, the distances between phase interfaces and fine/coarse boundaries [see L_i^* in Fig. 2(b)] continue to change. Since a too large L_i^* [too large size of the HRG layer, see also L_2^* and L_4^* in Fig. 2(b)] can lead to unnecessary computational cost and a too small L_i^* [too small size of the HRG layer, see also L_1^* and L_3^* in Fig. 2(b)] can lead to loss of accuracy, the actual distance L_i^* should be kept within an appropriate range. In our SDG AMR, if L_i^* deviates from the pre-determined range of $L_i \pm b_i$ (b_i is the allowable offset from the fine/coarse boundary in each direction), L_i^* is re-initialized as L_i in the re-grid procedure [compare the gray thick dotted lines and the green thick solid lines in Fig. 2(b)]. Hence, each distance between the interface and the fine/coarse boundary (L_i^*) is always ensured to be in the range of $L_i \pm b_i$.

If the HRG layer is expanded after the re-grid procedure [see black thick arrow in Fig. 2(b)], a new section of the domain will be added to the HRG [see orange HRG area outside the gray thick dotted lines in Fig. 2(b)]. In this case, the velocity and pressure fields at the added domain need to be initialized. As in many existing AMR techniques (Griffith *et al*., 2007; Sussman *et al*., 1999; Usui *et al*., 2014), the initial values for the added domain are obtained by interpolating values from the LRG layer. The interpolation procedure becomes important because it directly affects the accuracy of solutions of the HRG layer. Several interpolation schemes from first-order linear to third-order spline have been applied for such an initialization of the added domain in many previous studies (Griffith *et al*., 2007; Sussman *et al*., 1999; Usui

et al., 2014). Here we select the third-order cubic spline similar to the boundary condition implementation for the HRG layer. Another important factor to ensure an optimal condition for the re-grid procedure is the choice of allowable offsets b_i. If too small a value of b_i is applied, the re-grid becomes too frequent thus numerical errors caused by the interpolation can accumulate even though the computational cost for the HRG layer can be somewhat reduced. Therefore, an optimal condition for b_i should be ensured. We performed extensive preliminary tests and these test results of re-grid characteristics will be explained later in detail.

D. Overall solution procedure

The governing equations, Eq.(1-2), are integrated in time using the projection method (Chorin, 1968) on a staggered grid (MAC method) (Harlow and Welch, 1965). A second-order essentially non-oscillatory (ENO) method (Shu and Osher, 1989) and standard central difference methods are used for the discretization of the convective and diffusive terms, respectively. The discrete form of Eq. (2) can be written as:

$$\frac{\mathbf{u}^{n+1}-\mathbf{u}^{n}}{\Delta t}=\frac{1}{\rho^{n}}\left(\mathbf{A}^{n}+\mathbf{F}^{n}\right)-\frac{1}{\rho^{n}}\nabla_{h}P \tag{14}$$

where the advection, diffusion, and gravitational terms in Eq.(2) are lumped into **A** for simplicity. The subscript *h* stands for a spatial discretization operator. Eq. (14) is split into:

$$\frac{\tilde{\mathbf{u}}-\mathbf{u}^{n}}{\Delta t}=\frac{1}{\rho^{n}}\left(\mathbf{A}^{n}+\mathbf{F}^{n}\right) \tag{15}$$

$$\frac{\mathbf{u}^{n+1}-\tilde{\mathbf{u}}}{\Delta t}=-\frac{1}{\rho^{n}}\nabla_{h}P \tag{16}$$

here, $\tilde{\mathbf{u}}$ is the new velocity field without regarding the pressure term. To enforce $\mathbf{u}^{n+1}$ to be divergence-free, the pressure field is obtained by solving:

$$\nabla_{h}\cdot\left(\frac{1}{\rho^{n}}\nabla_{h}P\right)=\frac{\nabla_{h}\cdot\tilde{\mathbf{u}}}{\Delta t} \tag{17}$$

Then the velocity field at the next time step is:

$$\mathbf{u}^{n+1}=\tilde{\mathbf{u}}-\frac{\Delta t}{\rho^{n}}\nabla_{h}P \tag{18}$$

The time-step size, Δt, is adaptively computed in order to ensure that the Courant number is always less than 0.1 based on the grid size of the HRG layer and applied to both the HRG and LRG layers. Note that the governing equations are solved sequentially for each Eulerian grid layer and this value of the time-step is applied to both layers as in many existing AMR techniques (Fakhari and Lee, 2014; Griffith *et al*., 2007; Popinet, 2003; Roma *et al*., 1999). Sub-cycling (Berger and Colella, 1989) which utilizes a smaller time step in the HRG layer has not been used. Sub-cycling is known to increase computational efficiency (Ceniceros *et al*., 2010; Roma *et al*., 1999) in some applications but we find that it has minimal effect in the current study of droplet-particle interaction in mid-air.

The overall simulation procedure can be summarized as follows:

1. Initialization

i) Eulerian grid generation for the LRG layer

ii) Lagrangian grid generation for the (fluid-fluid) phase interface

iii) ϕ_s field generation for the (fluid-solid) phase interface

iv) Eulerian grid generation for the HRG layer

2. Time integration loop

i) solving dynamic contact angle (Eq.11)

ii) call modularized solvers (once for each layer) for the governing equations

a) module#1: calculation of the distance functions (ϕ_f, ϕ_s) and indicator functions (I_f, I_s)

b) module#2: calculation of the physical properties (Eq.3-4)

c) module#3: calculation of the surface tension force (Eq.5-8)

d) module#4: projection for calculation of **u** and p (Eq.14-18)

iii) interface advection using the velocity field of the HRG layer

a) calculation of the contact line velocity (Eq.10)

b) fluid-fluid interface advection (Eq.9)

c) solid-fluid interface advection (Eq.12-13)

iv) Lagrangian interface reconstruction (under certain conditions if needed)

v) HRG layer re-grid (under a certain conditions if needed)

Our proposed SDG AMR technique is quite similar to a patch-based AMR (Berger and Colella, 1989; Griffith *et al*., 2007; Roma *et al*., 1999) regarding two aspects: (i) different computational domains are connected by the boundary conditions and (ii) the fine/coarse boundaries are aligned with the grid lines of the domain that has the lower grid resolution. Indeed, the SDG AMR can also be interpreted as a simpler type of patch-based AMR in terms of the grid configuration. However, unlike that the boundary conditions are mutually

interchanged in the conventional patch-based AMR, only the boundary conditions of the LRG layer are transferred to the HRG layer in the SDG AMR. This means that the physical domain covered by the HRG layer is solved twice which can be considered as an efficiency loss in terms of the computational cost. On the other hand, the algorithm can be highly simplified with much easier implementation since the boundary conditions are unidirectionally transferred from the LRG layer to the HRG layer.

In order to transfer information from the HRG layer to the LRG layer, indexing for related cells is essential which cannot be done by simple recursive calls of an interpolation routine. Even though an implementation for such indexing is not so challenging in the current two-dimensional framework, it imposes significant complexity in the three-dimensional formulation. In fact, we have developed both versions [i.e. (i) boundary conditions interchanged between the HRG layer and the LRG layer (conventional patch-based AMR), and (ii) boundary conditions only unidirectionally transferred from the LRG layer to the HRG layer) and compared their numerical performance in terms of the computational cost and the solution accuracy (we discuss this comparison in section 3 in more detail). We concluded that the simpler implementation is more useful even here for two-dimensional simulations (i.e. simulations of the droplet-particle collision in mid-air) and certainly for future implementation to a three-dimensional parallelized framework.

The most distinctive (and as also intended) characteristics of the proposed SDG AMR are simplicity and scalability. Details are as follows:

i) Unlike the tree-based AMR (Fakhari and Lee, 2014; Popinet, 2003; Zuzio and Estivalezes, 2011), the governing equations can be solved without any additional modification of existing codes. Existing array- and cache- based data structures are also applicable without change. Complex procedures for data handling, e.g.,

searching for neighbor cells or tree-searching are unnecessary. Load balancing for the parallel computations can be ideally performed as in the block type tree-based AMR (van der Holst, 2007) since the governing equations are separately solved at both the HRG and LRG layers.

ii) Grid configuration of the HRG layer and its re-grid procedure are significantly more simple and straightforward compared to the conventional patch-based AMR methods. Procedures for tagging cells to be refined (Berger and Colella, 1989; Griffith *et al*., 2007; Roma *et al*., 1999) or for point-clustering to optimize refined patches (Ceniceros, 2010a; Griffith *et al*., 2007; Roma *et al*., 1999) no longer exist. Since only the recursive interpolations for initializing **u** and p in the added domain are needed after the re-grid procedure, the computational cost for the re-grid steps is also negligible.

iii) The solutions for governing equations can be fully modularized. This enables the SDG AMR technique to be independent of the main solver for the Navier-Stokes equations including interface dynamics. Thus, maintenance or updates of the main solver can be done separately from the SDG AMR procedure. The current SDG AMR method can also be easily customized for a wide variety of simulations. For example, multiple HRG layers can be further introduced for certain cases (e.g., bubbly flows).

III. RESULTS AND DISCUSSION

Fig. 3 shows the simulation domains and boundary conditions used in the current study. A two-dimensional axisymmetric simulation is considered for all cases. Two Eulerian domains,

i.e. the HRG and the LRG layers are marked by orange and white regions, respectively. The lengths of the LRG layer which covers the physical domain in the radial (r) and axial (z) directions are R_L = 5 - 10 and Z_L = 20 - 40 times the droplet radius whereas the size of HRG layer can be continuously changed by the re-grid procedure depending on the motions of droplet and particle. The pressure boundary conditions are applied to all boundaries of the LRG layer except for the left boundary at which the axisymmetric boundary condition is applied. As explained in section 2.C, the boundary conditions for the HRG layer are obtained by interpolating the values of the LRG layer. Although the grid resolutions of the two layers can be chosen independent of each other, the grid resolution of the LRG layer is always set as half of the resolution of the HRG layer in each direction (r- and z-direction) for the current study.

A droplet collides on a dry, spherical particle and its impact velocity is denoted by V_{ini}. D_d and D_p are the diameter of the droplet and the particle, respectively. Note that the particle is stationary before the collision and it starts to move after collision, as in the recent experiment of Pawar *et al*. (2016). The physical properties of water and ambient air are used to describe the liquid and gas phase (ρ_d = 998.2 kg/m^3, μ_d = 0.001 N s/m^2, ρ_a = 1.2 kg/m^3, μ_a = 0.00018 N s/m^2). For the solid particle, ρ_p = 1602.0 kg/m^3, which is comparable with a common sand particle, and μ_p = 0.1 N s/m^2, which is 100 times the liquid viscosity, are used in this study to emulate rigid motion of the particle. The surface tension coefficient is set to σ = 0.0728 N/m.

To characterize the droplet collision behavior, two of three dimensionless numbers, i.e. Weber number (We = $\rho_d V_{ini}^2 D_d$ / σ), Reynolds number (Re = $\rho_d V_{ini} D_d$ / μ_d) and Ohnesorge number [Oh = μ_d / $(\rho_d \sigma D_d)^{0.5}$] are frequently used. We use the Weber number (which represents the inertial force relative to the surface tension force) and Ohnesorge number (which represents the viscous force relative to the inertial forces and the surface tension force) in the current study. The surface wettability is measured by the equilibrium contact angle θ_{eqi} and $\Omega = D_d/D_p$ is the droplet-to-particle diameter ratio.

It is well known that many variables (e.g., impact velocity, liquid viscosity, wettability and roughness of the surface, etc.) are involved in the droplet-particle collisions (Rioboo *et al.*, 2002; Roisman *et al*., 2002). Moreover, the physical phenomena associated with the collision in mid-air are even more complicated because of the motion of the particle. Therefore, we consider only head-on impact at this time to narrow our research scope. The droplet diameter D_d is fixed to be 2 mm as in our previous study (Yoon and Shin, 2021b) for direct comparison with the simulation results from the stationary particle counterpart. With the given droplet diameter (D_d = 2 mm), the Weber number (We) and the droplet-to-particle size ratio (Ω) are controlled by varying the impact velocity V_{ini} and the size of the target particle D_p. Since a water droplet is considered here for its versatility, the Oh is fixed as Oh = 0.0026. The initial deformation of the droplet before the collision and turbulent effects are not considered due to their negligible effects (Khurana *et al*., 2019; Pasandideh-Fard *et al*., 2002). The solid surface is assumed to be well prepared so contact angle hysteresis (CAH) of ±2.5° is applied for all cases. Note that the Bond number ($Bo = \Delta\rho g D^2/\sigma$), which compares the gravitational force to the surface tension force, is less than unity (Bo = 0.53). This means that the surface tension force can overcome the gravitational force, thus the recoiling motion (driven by the capillary effect) follows right after the inertia-driven spreading of the droplet.

A. Performance check of the SDG AMR technique

The performance and efficiency of the proposed SDG AMR strategy are evaluated in the context of simulation of droplet-particle collisions in mid-air. Note that our existing computational framework including the formulations of LCRM, FDM and dynamic contact angle modeling has been extensively validated with many experimental and theoretical studies on droplet impact with stationary and moving solid targets (Choi and Shin, 2019; Yoon and

Shin, 2021a, 2021b, 2021c). Therefore, we focus here on the computational performance of the proposed AMR technique by a comparison to the simulation results from a uniform fine grid without the AMR approach (i.e. the reference case). Note also that 'uniform fine grid' means 'uniform grid with mesh size of the HRG layer'.

Fig. 4 depicts grid convergence characteristics and computational costs. Droplet collision with a stationary target (We = 62.6, $\Omega = 0.5$, and $\theta_{eqi} = 40°$) is considered. For simulation cases with the SDG AMR, L_i (the clearance distance between the phase interfaces and the fine/coarse boundaries) and b_i (the allowable offsets from the fine/coarse boundaries) are set to $L_i = 0.2D_d$ and $b_i = 0.05D_d$, respectively (see Fig. 2(b)). The lengths of the LRG layer are set to $R_L = 6$ and $Z_L = 15$ times the droplet radius. In Fig. 4(a), typical interface evolution of the droplet is shown. The droplet severely deforms until the maximum spreading state (see $\tau = 3.75$) then the recoiling stage starts driven by the capillary force to reduce the surface energy (see $3.75 \leq \tau \leq 12.75$). The droplet falls downward again without the rebound behavior because the particle surface is hydrophilic ($\theta_{eqi} = 40°$), and reaches the equilibrium state (see $12.75 \leq \tau \leq 30.00$). Note that this is a simple collision case on a stationary particle but is one of the most dynamic cases because the initial impact Weber number (62.6) rapidly increases to 840 locally during the recoiling stage ($\tau \sim 6.75$) (Yoon and Shin, 2021b).

Fig.4(b) shows the temporal variation of the non-dimensional spreading diameter D^* ($D^* = D_{spread}/D_d$), where D_{spread} is defined as the wetted arc length of the droplet [see curved red arrow-line of the inset in Fig. 4(b)]. The blue, red, and black lines indicate the different grid resolutions of the HRG layer. The solid, dashed, and dotted lines indicate the results obtained using the uniform fine grid, using the SDG AMR without re-grid, and using the SDG AMR with re-grid, respectively. As seen, and as also shown in Yoon and Shin (2021b), grid convergence is nearly achieved at CPR = 32. It is also observed that the results obtained using the SDG AMR technique show sufficiently good agreement with the results of reference cases

obtained using the uniform fine grid regardless of the re-grid procedure, if the grid resolution of the HRG layer is sufficiently high (i.e. $CPR_{HRG} \geq 32$). This means that the SDG AMR can provide a nearly identical solution to the reference cases even though the grid resolution of the LRG layer is reduced by half.

In Fig. 4(c), we compare computational times (t_c) for cases shown in Fig. 4(b) above. All the simulations in this section were performed on a system equipped with two 4-core 3.60 GHz Intel® Xeon® X5687 processors. Each computational time is normalized by t_c of the reference case [$\tau_c = t_c / t_{c\,(ref)}$] and is presented above each bar. In the upper-right corner, a snapshot at the end of the simulation period is inserted to show the relative size of the HRG layer to the LRG layer. As seen, τ_c are reduced to 0.37 ($CPR_{HRG} = 32$) and 0.24 ($CPR_{HRG} = 64$), respectively, compared to the reference cases if SDG AMR is applied (without re-grid). One can find that the re-grid procedure has no meaningful effect on the additional decrease in the computational time here. Since a stationary target is being considered, only a minor optimization for the size of HRG layer occurs. Therefore, change in the size of the HRG layer is not notable during the simulation period and thus has a minimal effect on the computational cost.

As described above, the re-grid can play a decisive role in a simulation where the HRG layer needs to move along with target objects such as a collision in mid-air, and is expected to have a more notable effect on the decrease in computational cost. Frequent re-grid allows more efficient computation by minimizing the necessary size of the HRG layer but it might also lead to loss of accuracy due to the cumulated interpolation error. Therefore, effects from the re-grid frequency and interpolation scheme on solution behavior need to be investigated for a practical application in advance. Fig. 5 and Fig. 6 show the effects of re-grid frequency and interpolation scheme on the loss of accuracy. Three collision cases of droplet-particle collision in mid-air, i.e. We = 4, 67, and 200 are considered, and linear interpolation and third-order cubic spline interpolation are applied in Fig. 5 and Fig. 6, respectively. The non-dimensional spreading

diameter D^* and the non-dimensional lamella height H^* are used to characterize quantitatively the collision behavior. H^* is defined as $H^* = H / D_d$, where H is the length of the lamella [see blue arrow-line of the inset in Fig. 5(b)]. To control the re-grid frequency, we mainly vary b_i (the allowable offsets from the fine/coarse boundaries). ξ is introduced to measure the re-grid frequency and can be obtained by dividing the total number of re-grids performed by the total number of time-integrations during an entire simulation period. Therefore, $\xi = 1$ signifies that the re-grid procedure is performed at every time-step. In each figure, the simulation result from the uniform fine grid is inserted as a reference case (see black solid line). Note that dashed lines in Fig. 5 and Fig. 6 indicate results which fail to obtain a sufficiently identical trend to the reference cases. Grid resolution of the HRG layer is $CPR_{HRG} = 32$ whereas $\Omega = 1.0$ and $\theta_{eqi} = 90°$. The lengths of the LRG layer are set to $R_L = 5$ and $Z_L = 20$ times the droplet radius, respectively.

It is natural that the re-grid frequency ξ increases in reducing b_i. If the linear interpolation scheme is used, as can be seen in Fig. 5, the results become evidently poor with relatively high ξ due to the cumulated interpolation error. Note that L_i (the clearance distance between the phase interfaces and the fine/coarse boundaries) is always fixed to $1.0D_d$ and this value is sufficiently large to ensure that its effect becomes negligible. For a collision at We = 4 [see Fig. 5(a)], simulation results with $b_i \leq 0.03D_d$ cannot reproduce the collision behavior correctly (See blue and yellow dashed lines). As We increases, such limitation of frequent re-grid becomes evident. Only a very small value of ξ ($\xi \leq 0.001$) is allowable if We ≥ 67 [see Fig.5(b) and (c)].

Simulation results using the third-order cubic spline interpolation are presented in Fig. 6. All impact conditions are the same as Fig. 5 but different re-grid conditions are used in Fig. 6. Note that all simulations were performed with a very small value of b_i ($b_i = 0.01D_d$), thus extremely frequent re-grid procedures were done, i.e. $\xi > 0.7$. As seen, most D^* and H^* results

show good agreement with the reference cases. Small deviations [e.g., $\tau \geq 4$ in Fig. 6(c)] are acceptable since all simulations in Fig. 6 were performed under the extremely frequent re-grid conditions ($\xi > 0.7$). Effects of the size of the HRG layer is also seen in Fig. 6. For a case with very small We (We = 4), very small size of the HRG layer ($L_i = 0.1D_d$) is sufficient. However, the results with $L_i = 0.1D_d$ lead to some deviations which cannot be negligible if We = 67 and 200 [see blue dashed lines in Fig.6(b) and(c)], even though their trends are qualitatively identical to the reference cases. This means that larger L_i is needed to properly capture the collision behavior as Weber number increases. We performed various tests and concluded that $L_i = 0.3D_d$ is reasonable within a range of collision conditions considered herein (but we use $L_i = 0.5D_d$ for the practical simulations in section 3.B to be on the safe side). Two dotted boxes are also inserted in each case to show the interfacial morphologies of droplets and particles (the particles are marked by a letter 'p'). Black lines indicate the reference cases whereas red lines indicate the cases from $L_i = 0.1D_d$, $L_i = 0.3D_d$, and $L_i = 0.5D_d$ in Fig. 6(a), (b), and (c), respectively. As seen, interfacial morphologies also show good agreement with the reference cases. We conclud that a high order interpolation scheme is essential for the SDG AMR procedure.

Fig.7 and Table.1 present how much the computational cost can be reduced by using the SDG AMR. The computational times for three collision cases shown in Fig. 6 are compared. To present the relative size of the HRG layer to the LRG layer, snapshots near the end of the simulation period are inserted at the right side of each case. Overall, we observed that the computational times decreased to 13 – 15 % compared to the reference cases simulated using the uniform fine grid. We also expect that such benefits can be further increased for three-dimensional simulations. Note that the proposed SDG AMR is developed for a specific situation where the localized area of interest moves dynamically in a large physical domain to reduce the effect from ambient boundary conditions. It is evident that for a smaller relative

size of the HRG layer covering the target region of interest to the size of LRG layer, the computational benefit becomes larger. In a three-dimensional simulation of droplet-particle collision, the target geometry occupies a much smaller region compared to a two-dimensional simulation and thus the computational cost can be expected to decrease further significantly.

We showed results of the performance of the proposed SDG AMR technique above in terms of the accuracy and cost-efficiency. Since two different grids are synchronously solved, it is important to ensure a divergence-free condition over the boundaries between the HRG and the LRG layer (i.e. at the fine/coarse boundaries). The net value of the fluid flux at the fine/coarse boundaries should be zero because the flow is incompressible. However, such net-flux never reaches an exact zero due to the numerical errors (e.g., the truncation error) even with a uniform fine grid without an AMR approach. Fig. 8 shows typical net-flux errors at the fine/coarse boundary (the collision conditions are the same as Fig.4). The cumulative net flux difference between the SDG AMR approach and the reference case obtained using the uniform grid is normalized again with the reference value. As can be seen from Fig. 8, these normalized net-flux differences are generally on the order of $O(10^{-6})$ during the entire simulation period if cubic spline interpolation is applied. This signifies that the flux error caused by our proposed SDG AMR can be maintained at a negligible level without any extra procedures for ensuring divergence-free flow such as an additional projection step (Ceniceros *et al*., 2010b).

Lastly, it is also worthwhile to mention that we also compared two strategies in terms of the treatment of the overlapping domain of the HRG layer with the LRG layer. As described above, in the SDG AMR approach, the governing equations are first solved at the LRG layer then are solved again at the HRG layer using the boundary conditions obtained by interpolating the values at the LRG layer. This means that the physical domain covered by the HRG layer (overlapping domain) is solved twice and naturally leads to some loss of computational efficiency. A different approach can also be considered where only the LRG layer outside the

HRG layer is solved using boundary conditions from the values of the HRG layer. Thus fine/coarse boundaries are coupled as in the conventional patch-based AMR procedure (Berger and Colella, 1989). An apparent advantage would be more efficient computation since the overlapping domain can be solved just once. However, additional implementations for complicated indexing are also necessary to adopt the second strategy. We compared the two strategies in terms of the accuracy and computational efficiency. From several tests, we concluded that the computational cost can be further decreased by about 10 – 25 % globally with the second strategy but a remarkable improvement of accuracy cannot be found. Since the first strategy showed sufficiently reasonable result for the simulation of droplet-particle collision in mid-air, and to avoid additional implementation complexities, we chose to use the first strategy. It is also expected that such a choice could provide a more desirable environment for expanding the current SDG AMR procedure to a three-dimensional parallelized framework due to its simplicity.

B. Simulation of droplet-particle collision in mid-air

In this section, we systematically analyze the different physical characteristics between two droplet-particle collision systems (i.e. droplet-particle collision in mid-air and collision with a stationary particle) by comparing the impact outcomes and underlying mechanisms.

To compare the impact outcomes in mid-air with the existing results obtained on a stationary particle (Yoon and Shin, 2021b) for a wide range of collision conditions, we consider 9 cases of impact velocity V_{ini}: 0.38, 0.60, 1.05, 1.35, 1.60, 1.81, 2.00, 2.18, 2.34 m/s. Such a V_{ini} range corresponds to a Weber number range of $4 \leq We \leq 150$. Note that $We \sim 150$ is near the splashing threshold for a droplet collision with a stationary particle (Hardalupas *et al.*, 1999; Yoon and Shin, 2021b). We also consider 5 cases of equilibrium contact angle θ_{eqi}: 20°, 55°,

90°, 125°, 160° to cover a wide range of surface wettability, from hydrophilic to super-hydrophobic surfaces.

A broad range of droplet-to-particle size ratios Ω can be found in practical engineering applications [e.g., $0.2 \leq \Omega < 2.0$ for a spray dryer producing milk powder (Pawar *et al*., 2016)] and the collision phenomena significantly diverge near the critical size ratio (Ω_c) of 0.6 - 0.67 because a particle can be completely coated by a droplet when $\Omega > \Omega_c$ (Khurana *et al*., 2019; Yoon and Shin, 2021b). For a small Ω ($\Omega < \Omega_c$), partial coating outcomes (e.g., deposition or rebound) are mainly observed whereas coating outcomes (e.g., complete coating or lamella disintegration) are mainly observed for opposite cases ($\Omega > \Omega_c$) (Yoon and Shin, 2021b). To examine the collision characteristics for both cases, 2 representative cases of Ω (0.5 and 1) are considered. Hence, the collision conditions cover 90 cases (9 impact velocities, 5 surface wettabilities, and 2 droplet-to-particle size ratios) for each system (collision in mid-air and collision with a stationary particle). Since the simulation results became converged near a grid resolution of CPR_{HRG} = 32 (see Fig.4), we used a grid resolution of CPR_{HRG} = 64 for all simulation cases hereafter to be on the safe side.

Fig. 9 compares the outcome regime maps between two collision systems. Two outcome regime maps for the collisions with a larger particle (Ω = 0.5) are illustrated on the upper side, whereas the other two regime maps for the collision with a smaller particle (Ω = 1) are placed on the lower side. The results for the collision with a stationary particle (Yoon and Shin, 2021b) and the results for the collision in mid-air (currently simulated) are depicted on the left and right sides, respectively. In each regime map, the impact Weber number ($4 \leq We \leq 150$) and the equilibrium contact angle ($20° \leq \theta_{eqi} \leq 160°$) are also plotted in the vertical and horizontal directions.

Here we briefly introduce the typical impact outcomes from the droplet-particle collision (Yoon and Shin, 2021b). The impact outcomes can be categorized into seven typical regimes:

deposition (DP), partial rebound (PR), complete rebound (CR), complete coating (CC), gravity disintegration (GD), momentum disintegration (MD), and splashing (SP). Their representative snapshots are illustrated on the top side in Fig. 9 and each outcome is marked by different color in the regime maps. DP (red) shows a gentle deposition on the particle. PR (orange) and CR (yellow) reveal that the droplet is rebounded on the particle surface. CC (blue) is full coating where the droplet completely wets the particle without any disintegration. GD (sky-blue) and MD (light blue) are characterized by stretching of the lamella and its disintegration caused by gravity (GD) and momentum (MD), respectively. In fact, a detailed simulation of SP (gray) is very challenging due to its three-dimensional nature (e.g., crown structure, cusp and fingering) by the current axi-symmetric formulation (Zhang *et al*., 2016; Banitabaei and Amirfazli, 2020; Yoon and Shin, 2021b). Hence, as in the simulation of Zhang *et al*. (2016), SP was defined as "thinning and disintegration of the spreading lamella with satellite droplets taking off from the particle surface in the first spreading stage" (Yoon and Shin, 2021b). Excepting SP, six outcomes can be also categorized into two groups: partial coating group (DP, PR, and CR) and coating group (CC, GD, and MD). The partial coating group shows that the droplet covers only a fraction of the particle whereas the coating group shows that the particle is entirely wetted by the droplet. As can be seen in Fig. 9, the partial coating group outcomes (DP, PR, and CR) are observed with the larger particle [see Fig. 9(a) and (b)] whereas the coating group outcomes (CC and MD) are mainly observed with the smaller particle [see Fig. 9(c) and (d)]. GD is very difficult to occur under the collision conditions considered herein. Note that three additional cases (We = 20 and $\theta_{eqi} = 90°$, We = 25 and $\theta_{eqi} = 125°$, and We = 25 and $\theta_{eqi} = 160°$, and $\Omega = 1$ for all three cases) were simulated and their outcomes were also depicted in Fig. 9(c) to clarify the boundary of coating/partial coating regime. More detailed explanation and physical mechanisms for those seven collision outcomes can be found in Yoon and Shin (2021b).

For the collisions with a stationary particle, although both the surface wettability and the

Weber number affect the final outcomes for a given particle size, the surface wettability plays a greater role in determining the final outcomes (DP, PR, and CR) in the partial coating group [see Fig. 9(a)] whereas the Weber number plays a more decisive role in the coating group [see Fig. 9(c)]. However, for the collision in mid-air, their outcome distributions considerably differ from those on a stationary particle. We present three major different collision characteristics observed in the outcome regime maps as follows.

The first change is expected and is also not difficult to understand. For a droplet impact with a stationary target, as the droplet deforms and spreads over the particle, the initial impact (kinetic) energy is transformed into the surface energy. The viscous dissipation also affects the collision behavior but the spreading of the droplet is controlled by a capillary-limit under such low Ohnesorge number (Oh = 0.0026) (Bartolo *et al*., 2005; Clanet *et al*., 2004; Yoon and Shin, 2021c). Therefore, both the spreading and recoiling stages are mainly driven by the interplay between the inertial and capillary effects (Bartolo *et al*., 2005). Conversely, for a droplet-particle collision in mid-air, as the droplet pushes the particle, the impact momentum of the droplet is transferred to the particle and the initial impact energy of the droplet is less efficiently transformed into surface energy (the initial momentum cannot be completely used for spreading). Hence, the spreading momentum is reduced and a stronger impact energy (typically higher impact velocity) is required to show a similar amount of spreading compared to the collision with a stationary particle. Such change is clearly seen for both larger and smaller particles. For the case of a stationary target, the splashing threshold was observed near We ~ 150 with $\Omega = 1/2$ and $90 \leq We \leq 130$ with $\Omega = 1$ [see black thick dashed line in Fig. 9(a) and (c)]. However, such a splashing threshold is not seen for the collision in mid-air with $\Omega = 1/2$ [see Fig. 9(b)] and is only seen when the droplet collides with a superhydrophobic particle ($\theta_{eqi} = 160°$) with $\Omega = 1$ [see Fig. 9(d)]. The boundary of the coating/partial coating regime is also changed. When the collision occurs in mid-air, this boundary moves from $4 \leq We \leq 25$ to $30 \leq$

We ≤ 50 [compare green thick dashed lines in Fig. 9(c) and (d)]. Such changes in the splashing threshold and the boundary of the coating/partial coating regime mean that higher impact We is required to observe the splashing outcome (or to observe the coating group outcomes) if the collision occurs in mid-air, due to the reduced spreading momentum (reduced inertial effect for the spreading). One can find an interesting point: the splashing still takes place with θ_{eqi} = 160° and Ω = 1 when We ≥ 90, even though it cannot be observed with any other collision conditions [see Fig.9(d)]. Such characteristics imply that the hydrophobicity affects the decrease in spreading momentum in mid-air (we address this point later in detail).

The second change in the outcome regime maps is also seen. For a droplet collision in mid-air, the rebound is significantly promoted compared to the collision with a stationary target [compare green thick dashed lines in Fig. 9(a) and (b)]. The partial rebound outcome has not been observed with a (stationary) hydrophilic particle (θ_{eqi} ≤ 55°) but is always seen if θ_{eqi} ≤ 90° and We ≥ 50 in mid-air. The complete rebound is also promoted [see the cases with We = 4, θ_{eqi} = 125°, and Ω = 1/2 in Fig. 9(a) and (b)]. Conversely, the deposition outcome is very difficult to observe compared to the collision with the stationary particle. Such change has an important meaning especially in practical engineering of an encapsulation process because the complete deposition of coating agent is more challenging for the collision in mid-air (only a portion of the droplet would be used for complete coating resulting in some excess unused droplet material). This result also suggests that the recoiling dynamics as well as the spreading behavior is significantly affected by the motion of the particle.

The third change in the outcome regime map is unexpected and interesting. The direction of the boundary between coating/partial coating is changed. For a collision with a stationary particle, this boundary was formed nearly along two cases: from the case with We = 4 and θ_{eqi} = 20° to the case with We = 25 and θ_{eqi} = 160° when Ω = 1 [see thick green dashed line in Fig.9(c)]. The complete coating outcome can be achieved with relatively lower impact Weber

number on the hydrophilic particles compared to the hydrophobic particles, due to more energetically favored spreading characteristics on the wettable surfaces (Banitabaei and Amirfazli, 2017; Yoon and Shin, 2021b). Conversely, for a collision in mid-air, this boundary is formed somewhat interestingly [see thick green dashed line in Fig. 9(d)]. As seen, relatively higher impact We is needed to observe the complete coating outcome on the hydrophilic particle, compared to the hydrophobic target (compare the case with We = 30 and θ_{eqi} = 160° to the case with We = 50 and θ_{eqi} = 20°). In other words, complete coating can be achieved with relatively lower impact Weber number on the hydrophobic particles. This can be somewhat unfamiliar since the coating process is generally easier on wettable surfaces for a stationary target. The reason for which lower impact We is needed to observe the complete coating on the hydrophobic target in mid-air is the different amount of reduced spreading momentum between the hydrophilic and the hydrophobic particles. Therefore, such change in the boundary of coating/partial coating also implies that the surface wettability (hydrophobicity) affects the decrease in spreading momentum.

We now discuss the physical mechanisms that drive three changes described above in detail. Fig.10 compares two collision scenarios to show the underlying mechanism leading to the first change, i.e. reduced spreading momentum at the collision in mid-air. The evolutions of interface morphology are presented for two collision systems, i.e. collision with a stationary particle [Fig. 10(a)] and collision in mid-air [Fig. 10(b)]. Since all other collision conditions are the same for each case (We = 50, Ω = 1, and θ_{eqi} = 20°), their different collision characteristics are apparently caused by the motion of the particle. For a collision with a stationary target, the droplet spreads over the particle ($\tau \leq 1.82$) then the lamella merges again underneath the particle and the particle is completely wetted by the droplet (τ = 2.09). Afterward, the lamella is stretched, forming a ligament due to its strong impact momentum and inertial effect (τ = 3.11). This ligament continues to be elongated (τ = 6.41) and is finally

disintegrated owing to the surface tension force (τ = 8.17). It is not difficult to expect that the dominant effect driving this outcome (i.e. the momentum disintegration) is the strong inertial effect and impact momentum (Yoon and Shin, 2021b). Conversely, for a collision in mid-air, although the particle is completely wetted by the droplet (τ = 3.11), an elongated ligament and its disintegration are not seen (τ = 6.41) thus the outcome is finally observed as complete coating (τ = 8.17). Since the impact momentum of the droplet is transferred to the particle, its spreading momentum is reduced. Therefore, the droplet cannot form a ligament because the inertial effect is insufficient to overcome the capillary force which pulls the lamella upward to the particle. Moreover, the coating time, which can be defined as the time required for the droplet to completely cover the particle, also increases for the collision in mid-air (compare two cases at τ = 2.09).

We analyze quantitatively how the maximum spreading of droplet (D^*_{max}) is reduced in mid-air compared to the collisions with a stationary particle. In Fig. 11, D^*_{max} of two collision systems are compared for a wide range of We ($4 \leq We \leq 130$). Ω and θ_{eqi} are 0.5 and = 90°, respectively. As seen, D^*_{max} from the collision with a stationary target increases with Weber number along the scaling curve $D^*_{max} \sim 0.9We^{0.32}\Omega^{0.2}$ (Yoon and Shin, 2021c, see green dashed line). On the other hand, D^*_{max} from the collision in mid-air is reduced by about 18.3 – 29.1 % compared to the collision with a stationary particle, even though their global trend is qualitatively similar. It is also observed that the difference in D^*_{max} between those two systems increases with the Weber number.

Fig. 12 shows the underlying mechanism leading to the second change, i.e. the promotion of droplet rebound at the collision in mid-air. The collision case with a stationary particle and the case in mid-air are depicted in Fig. 12(a) and (b), respectively. Different behaviors between the two systems are also apparently caused by the motion of the particle because all other collision conditions are the same (We = 50, Ω = 1/2, and θ_{eqi} = 20°). For a stationary target,

the droplet reaches the maximum spreading state (τ = 3.11) then starts the recoiling process. The film thickness at the apex point is minimized (τ = 6.95) during the recoiling stage and rises again due to its upward motion (τ = 12.62) triggered by a V-like cusp near the collision center (τ = 6.95) (Yoon and Shin, 2021a). Since the droplet is restricted by the surface tension owing to a small contact angle at the hydrophilic surface, it falls again without the rebound on the surface (τ = 13.84). Conversely, for a collision in mid-air, the droplet is more elongated at the recoiling stage because the particle is moving in the downward direction (τ = 6.95). Since the contact line continues to move in the opposite direction to the upper part of the droplet, the elongated part of the droplet is disintegrated due to the surface tension force (τ = 12.62) and the droplet finally shows the partial rebound outcome (τ = 13.84).

Several apparent differences between the two systems can also be found in Fig. 12. The interfacial morphology at the maximum spreading state is significantly different. For a collision with a stationary particle, the droplet mass is squeezed into thin liquid lamella bounded thick rims and the film thickness measure at the collision center (at the apex point) is very thin [see τ = 3.11 in Fig. 12(a)]. However, for a collision in mid-air, the film thickness at the apex point is much thicker and considerable liquid mass is cumulated at the central part of the droplet [see τ = 2.30 in Fig. 12(b)]. A notable difference in the interfacial morphology is also seen at the minimum film thickness state. For a collision in mid-air, the recoiling rims are much thicker [see τ = 3.92 in Fig. 12(b)] compared to the collision with a stationary particle [see τ = 6.95 in Fig. 13(2)].

Fig. 13 quantitatively compares temporal variations of the non-dimensional spreading diameter (D^*) and the non-dimensional film thickness at the apex point (h^*) of the droplet between the two collision systems shown in Fig. 12. In addition to D^*, the maximum spreading time (τ_{max}), which can be defined as the time required to reach the maximum spreading state, is also decreased from τ = 3.11 to τ = 2.30 in mid-air [see Fig. 12 and Fig. 13(a)]. Due to volume

conservation, the decrease in D^* naturally implies an increase in h^* in mid-air. As can be seen in Fig.13(b), at the initial deformation period ($0 < \tau < 0.7$), h^* of the two systems are identical to each other following the universal trend that can be correlated by $h^* = 1 - \tau$ (Bakshi *et al.*, 2007; Mitra *et al.*, 2017; Yoon and Shin, 2021b; see green dashed line). However, those two curves diverge near $\tau \geq 0.7$ and h^* of the collision in mid-air is mostly thicker than collision on a stationary target. The time for the minimum film thickness is also reduced from $\tau = 6.95$ to $\tau = 3.92$ in mid-air [see Fig. 12 and Fig. 13(b)]. Finally, h^* on the stationary particle decreases again after the first recoiling stage (see $\tau > 12.62$), since the droplet cannot rebound on the particle. Conversely, h^* of the collision in mid-air shows no meaningful decrease due to the separation of the film in mid-air [see marker × in Fig. 13(b)].

Fig. 14 presents the two cases of collision in mid-air to show the third change, i.e. the phenomena that complete coating can be achieved with relatively lower impact energy on hydrophobic particles. Fig. 14(a) and (b) depict collisions with a hydrophilic ($\theta_{eqi} = 20°$) and a hydrophobic ($\theta_{eqi} = 160°$) particle, respectively. The other collision conditions are the same (We = 30 and $\Omega = 1$). For a collision with a hydrophilic target, the collision scenario seems to be basically similar to the case described in Fig. 12(b). However, the underlying physics leading to such a collision outcome (i.e. the partial rebound) contains the complicated effects of two mechanisms described above (Fig. 10 and 12). As seen in Fig. 14(a), the droplet exhibits the recoiling stage (see $\tau \geq 2.51$) because it cannot completely coat the particle due to the reduced spreading momentum (see Fig. 10-11 and related explanation about the mechanism for reduced spreading momentum in mid-air). Note that the droplet showed the coating (momentum disintegration) outcome with the same collision conditions (We = 30, $\Omega = 1$ and $\theta_{eqi} = 20°$) if the collision occurs on a stationary target [see Fig. 9(c)]. Afterward, the droplet is disintegrated due to the motion of the particle (see Fig. 12-13 and related explanation about the mechanism for promotion of rebound in mid-air) and finally shows the partial rebound

outcome (τ = 11.45). Conversely, as seen in Fig. 14(b), for a collision with a hydrophobic particle, the droplet can completely coat the particle (τ = 7.48). Note that the impact outcome on a stationary target under the same collision conditions (We = 30, Ω = 1 and θ_{eqi} = 160°) was the momentum disintegration [see Fig. 9(c)]. Although the outcome is changed to complete coating in mid-air due to the reduced spreading momentum, those outcomes are still in a coating group. This signifies that the spreading momentum is less reduced on the hydrophobic particle compared to the hydrophilic particle.

As seen in Fig. 14 [and as also seen in Fig. 9(d) with an explanation about the effect of hydrophobicity on the change in splashing threshold in mid-air], the decrease in spreading momentum in mid-air is affected by the surface wettability. This implies that the momentum transfer from droplet to particle depends on the wettability of the target surface. Such characteristics also lead to the somewhat unexpected impact outcomes in mid-air under certain collision cases: the droplet can be rebounded on a hydrophilic particle but it can completely coat the hydrophobic particle. However, how the surface wettability affects the momentum transfer at the initial period of collision is still difficult to describe explicitly. Several possibilities and their complicated interplay can be expected as a mechanism for such effect of surface wettability on the momentum transfer.

On the curved surface, the direction of the capillary force acting in the vicinity of the inner region (Šikalo *et al.*, 2005) of contact line can differ. For a collision with a flat surface, as can be seen in Fig. 15(a), this capillary force only has the horizontal directions (i.e. outward or inward directions). However, for a collision with a spherical target, the vertical components of the capillary force also play a role. As seen in Fig. 15(b), for a collision with a hydrophilic particle, the direction of capillary force is downward thus the droplet tends to push the particle during its spreading (see blue arrows). Conversely, for a collision with a hydrophobic particle, the direction of capillary force is upward and the particle tends to be pulled by the droplet (see

red arrows). Note that the capillary force can play a non-negligible role in the droplet spreading even under the relatively large Weber number because the inner region in the vicinity of the contact line is less affected by the inertial effect (Antonini *et al*., 2012; Šikalo *et al*., 2005). The experimental result of Sechenyh and Amirfazli (2016) also clearly showed that surface wettability played an important role in determining the impact outcomes as well as flow structure of droplet colliding with a particle in mid-air. Moreover, since the initial impact momentum is reduced due to the momentum transfer to the particle and is less efficiently used for the spreading itself, the relative importance of the capillary effect could increase in mid-air compared to the collision with a stationary target. A detailed analysis of the effect of surface wettability on the momentum transfer between the droplet and the particle is beyond the scope of the present study since our objective was to identify the key physical difference between two collision systems of droplet/stationary particle and droplet/moving particle. Detailed analysis of flow field inside the droplet and quantitative analysis (such as force analysis) would be our next step.

IV. CONCLUSION

In this study, we numerically investigate the droplet-particle collision in mid-air for a wide range of collision conditions ($4 \leq We \leq 150$, $20° \leq \theta_{eqi} \leq 160°$, and $\Omega = 1/2$ and 1). To understand the different physical behavior of two droplet-particle collision systems, i.e. collision in mid-air and collision with a stationary particle, a total of 90 cases were considered to build outcome regime maps and compared to the collision cases with a stationary target. The level contour reconstruction method (LCRM) (Shin and Juric, 2002, 2009) and the fictitious domain method (FDM) (Glowinski *et al*., 1999; Mirzaii and Passandideh-Fard, 2012) are

utilized to represent and to track the (fluid-fluid and fluid-solid) phase interfaces accurately. For an efficient numerical simulation of those complicated collision phenomena covering the extensively diverse collision cases, a simple but very useful adaptive mesh refinement (AMR) technique, i.e. Simple Dual Grid AMR (SDG AMR) is also proposed.

The proposed SDG AMR uses two Eulerian grid layers, i.e. HRG and LRG layers. The HRG layer uses a finer grid resolution and its domain size continues to change depending on the motion of the target area of interest, whereas the LRG layer uses a coarser grid resolution and a fixed domain size, covering the physical computational domain. The SDG AMR shows sufficiently identical results to those obtained using a uniform fine grid within a considerably reduced computational cost.

The present study reveals that the droplet-particle collision behavior in mid-air cannot be simply interpreted by extrapolating the collision results on a stationary particle. Three differences are clearly identified: for a collision in mid-air, (i) the spreading momentum is reduced compared to the collision with a stationary target, due to the momentum transfer to the particle. (ii) The rebound is promoted and the deposition outcome is very difficult to observe in mid-air because of the motion of the particle during its recoiling stage. (iii) The wetting characteristics change due to the different momentum loss behavior depending on the surface wettability of the target particle. Since the momentum transfer is affected by the wettability, some unexpected outcomes (the droplet can be rebounded on a hydrophilic particle whereas it can completely coat the hydrophobic particle) can also be observed in mid-air. In addition, the interfacial morphology, liquid mass distribution on the target, and the spreading time are all significantly changed on the moving target.

Further effort is needed to understand how the surface wettability affects the momentum

transfer between the droplet and particle in mid-air. The effect of particle mass on the collision dynamics will also need to be considered in the future study.

ACKNOWLEDGMENTS

This work is supported by Basic Science Research Program through the National Research Foundation of Korea (NRF) funded by the Ministry of Education (2017R1D1A1B03028518) and by the National Research Foundation of Korea (NRF) through grants funded by the Korean government (MSIT) (2020R1A2C1003822) and support through computing time at the Institut du Developpement et des Ressources en Informatique Scientifique (IDRIS) of the Centre National de la Recherche Scientifique (CNRS), coordinated by GENCI (Grand Equipement National de Calcul Intensif) Grant 2020 A0102B06721.

DATA AVAILABILITY STATEMENTS

Data sharing is not applicable to this article because no new data were created or analyzed in this study.

FIGURES

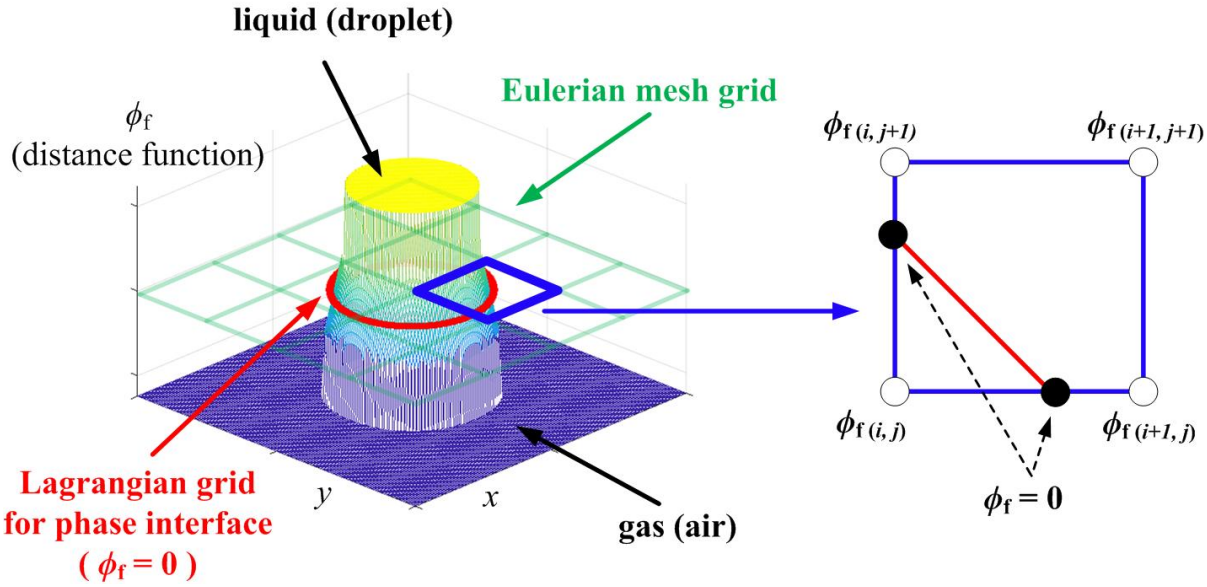

Fig. 1. General concept of the interface reconstruction in the LCRM. The phase interface can be represented by the distance function ϕ on the Eulerian (Cartesian) grid (green grid) as well as the Lagrangian moving mesh (thick red lines). The Lagrangian elements for the fluid-fluid phase interface are reconstructed on the cell faces of the Cartesian grid (blue grid).

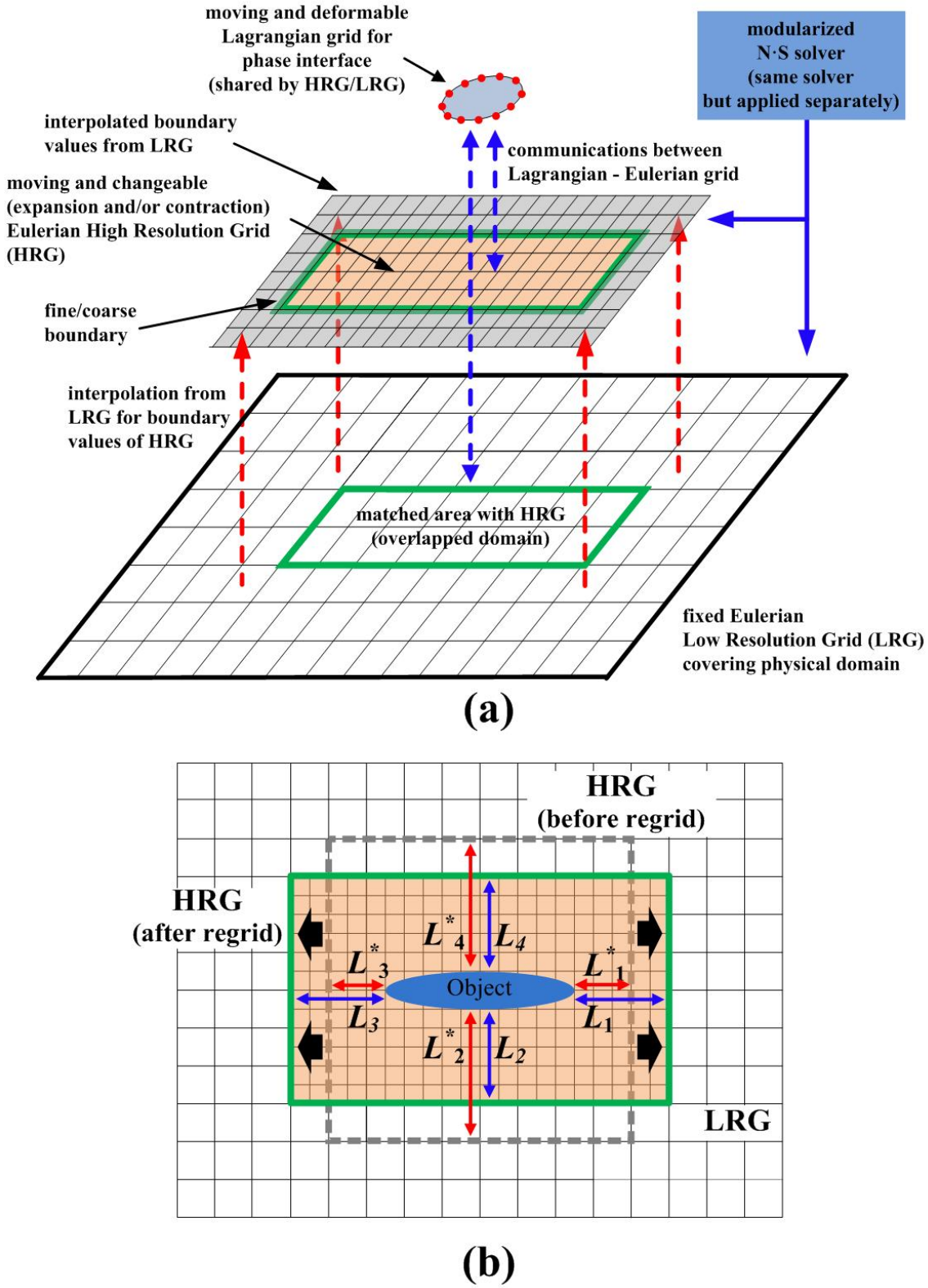

Fig. 2. (a) Basic concept of grid configuration in SDG AMR. Two Eulerian grid layers are simultaneously used. The HRG layer has a finer grid resolution (marked by the orange domain) and the LRG layer has a lower grid resolution (marked by the white domain). The boundary conditions for the HRG layer (marked by the gray zone) are obtained by interpolating the values at the LRG layer. The fluid-fluid phase interface is represented by moving Lagrangian grid (red dots). (b) Basic concept of re-grid for the HRG layer.

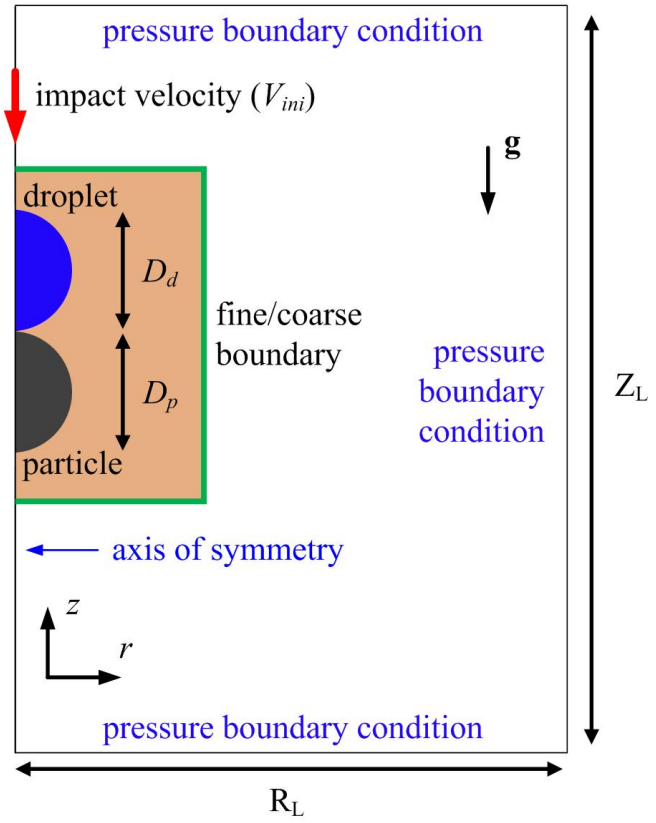

Fig. 3. Computational domain and boundary conditions for droplet-particle collision system using the SDG AMR strategy. Two Eulerian grids, i.e. the HRG layer (marked by the orange domain) and the LRG layer (marked by the white domain) are simultaneously used.

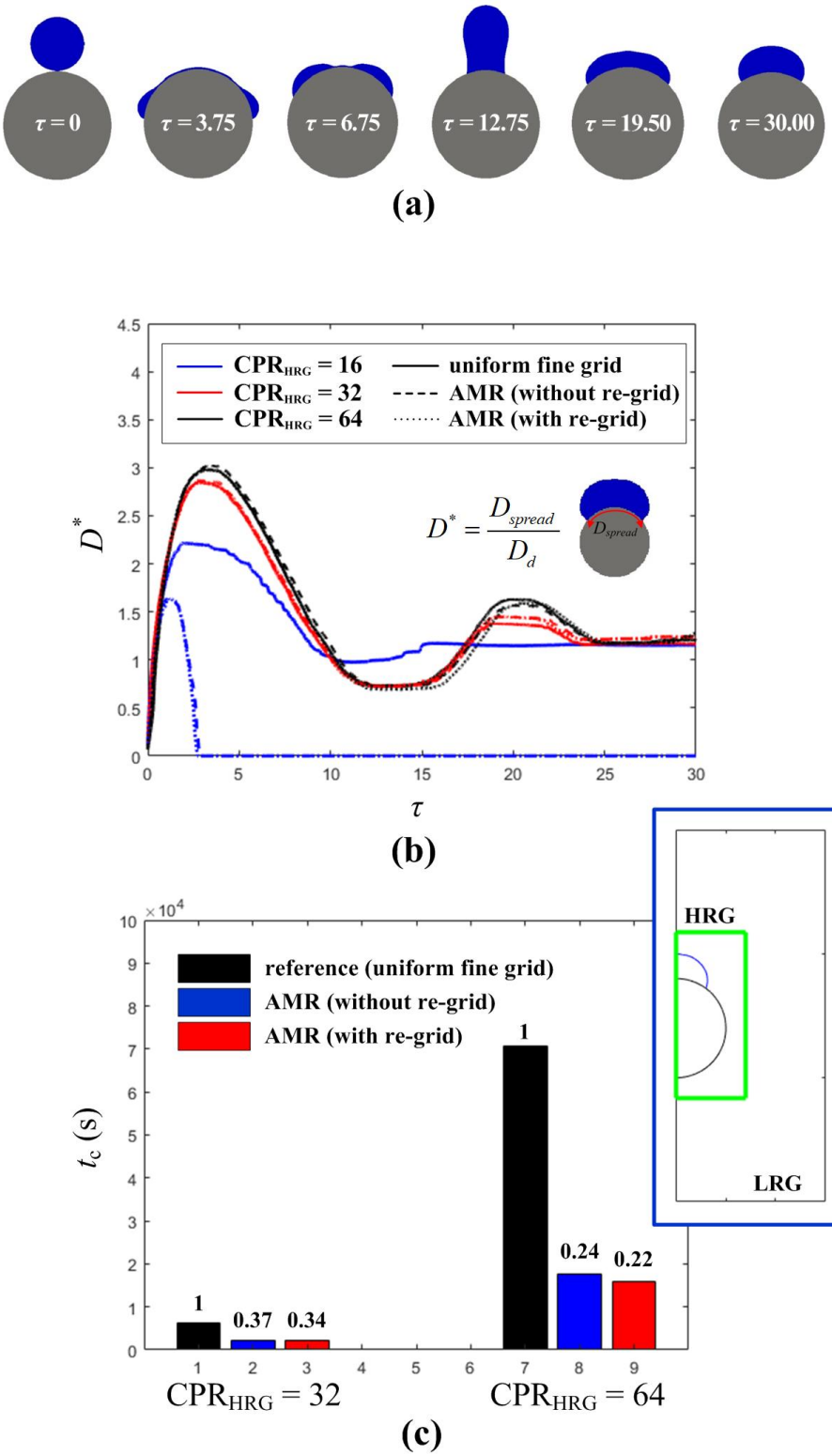

Fig. 4. Results of grid convergence test (We = 62.6, Ω = 0.5, and θ_{eqi} = 40°). (a) Evolution of interfacial morphology. The simulation case with SDG AMR (CPR_{HRG} = 64) is used for this illustration. (b) Non-dimensional spreading diameter D^*. The inset indicates the schematic diagram for measuring D^*. (c) Computational time t_c for each case. Normalized computational time τ_c is also shown above each bar. A snapshot at the end of the simulation is inserted in the upper-right corner to show the relative size of the HRG layer to the LRG layer.

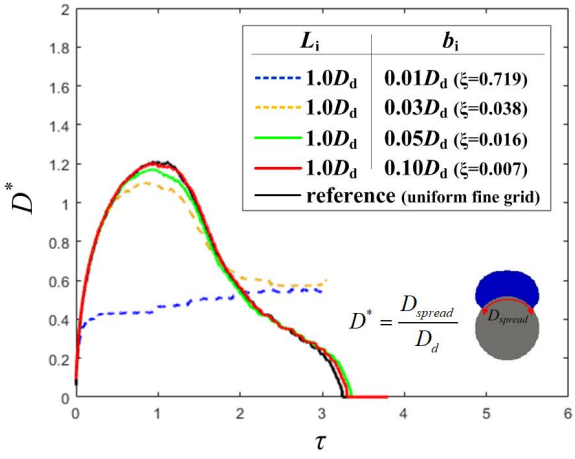

(a)

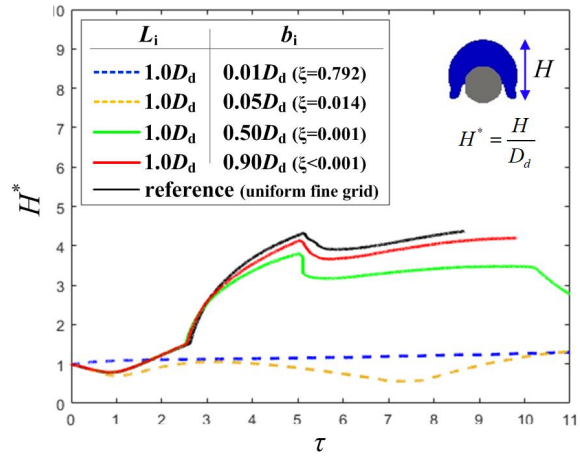

(b)

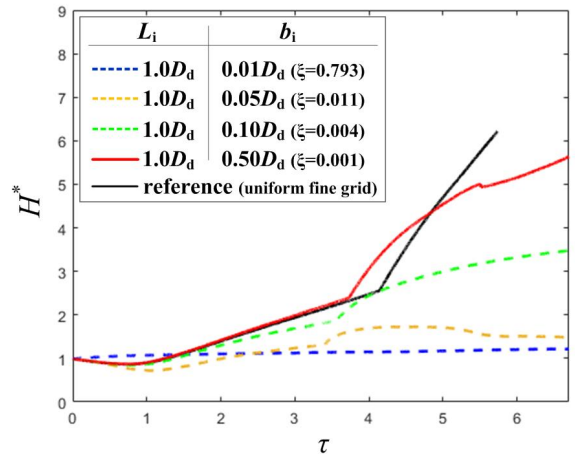

(c)

Fig. 5. Temporal variations of the non-dimensional spreading diameter D^* and the non-dimensional lamella height H^* from benchmark tests for different collision conditions and re-grid conditions. Linear interpolation is applied. (a) We = 4, (b) We = 67, and (c) We =200. The inset in Fig. 5(a) and (b) indicates the schematic diagrams for measuring D^* and H^*. Ω = 1.0 and θ_{eqi} = 90° for all cases.

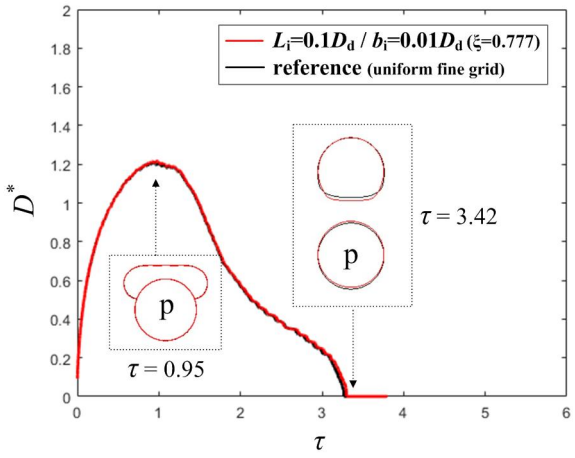

(a)

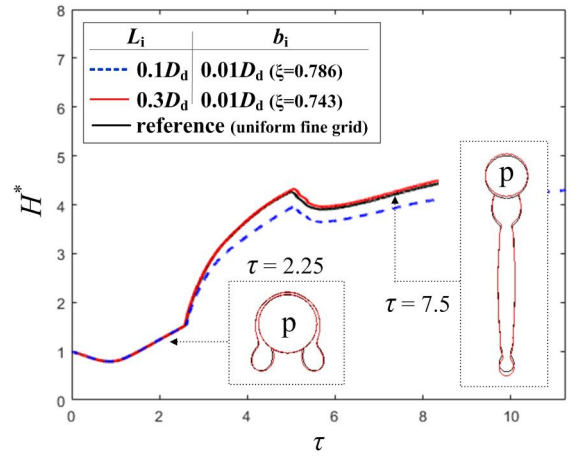

(b)

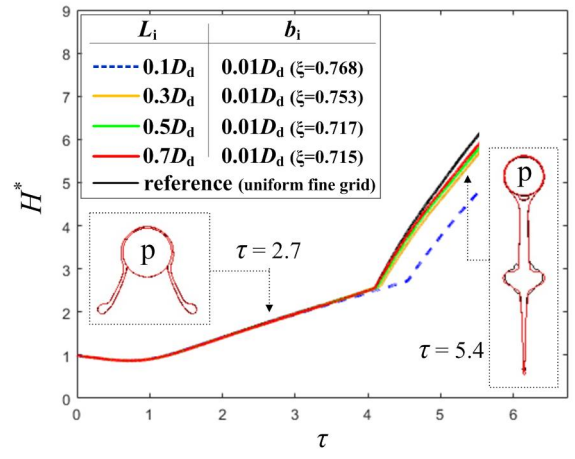

(c)

Fig. 6. Temporal variations of the non-dimensional spreading diameter D^* and the non-dimensional lamella height H^* from benchmarking tests for different collision conditions and re-grid conditions. Third-order cubic spline interpolation is applied. (a) We = 4, (b) We = 67, and (c) We =200. All simulations were performed under extremely frequent re-grid conditions ($\xi > 0.7$). $\Omega = 1.0$ and $\theta_{eqi} = 90°$ for all cases.

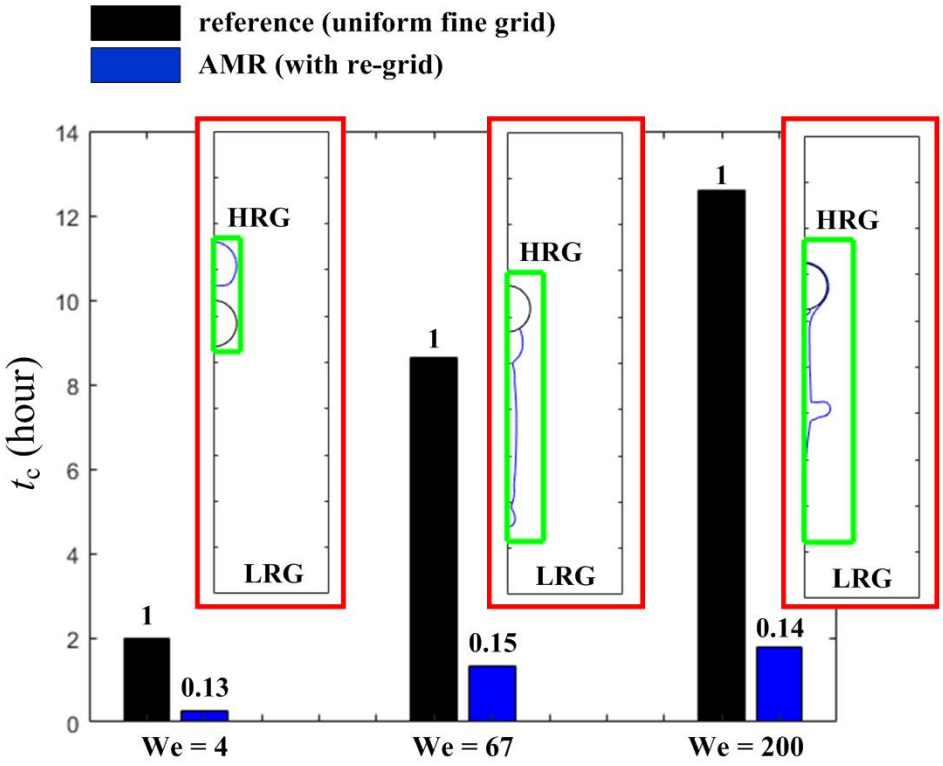

Fig. 7. Computational time t_c for the three collision cases (We = 4, 67, and 200). Normalized computational time τ_c is also shown above each bar. Snapshot near the end of the simulation is inserted at the right-upper side of each case to show the relative size of the HRG layer to the LRG layer.

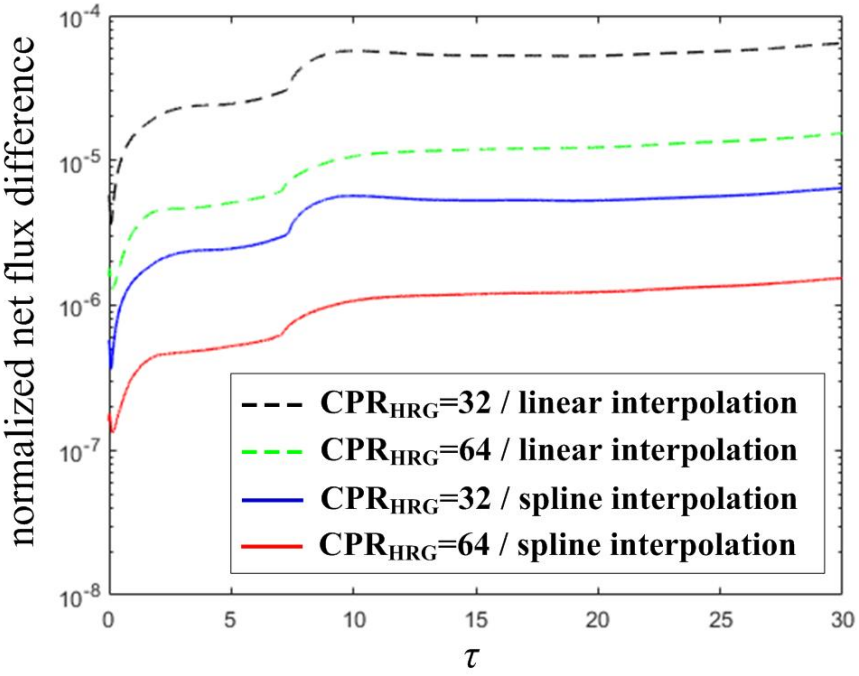

Fig. 8. Temporal variations of normalized net-flux difference (We = 62.6, Ω = 0.5, and θ_{eqi} = 40°).

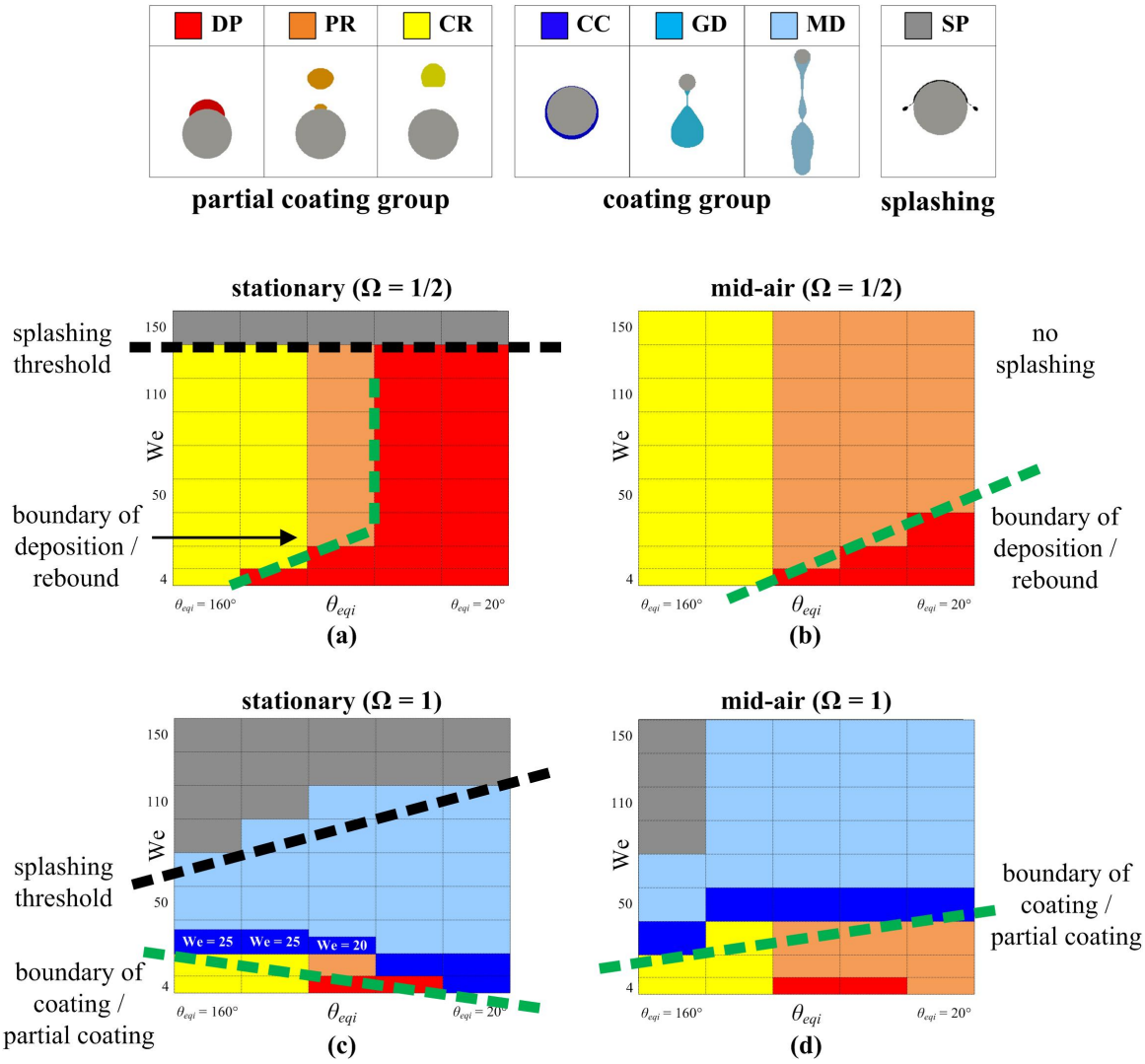

Fig. 9. Comparison of outcome regime maps. (a) outcomes from collision on a stationary particle (Ω = 1/2). (b) outcomes from collision in mid-air (Ω = 1/2). (c) outcomes from collision on a stationary particle (Ω = 1). (b) outcomes from collision in mid-air (Ω = 1). Typical outcomes are marked by different colors: deposition (DP, marked by red), partial rebound (PR, marked by orange), complete rebound (CR, marked by yellow), complete coating (CC, marked by blue), gravity disintegration (GD, not presented here), momentum disintegration (MD, marked by light blue), and splashing (SP, marked by gray). The Weber number (We = 4, 10, 30, 50, 70, 90, 110, 130, and 150) and the equilibrium contact angle (θ_{eqi} = 20°, 55°, 90°, 125°, and 160°) are plotted in the vertical and horizontal directions, respectively.

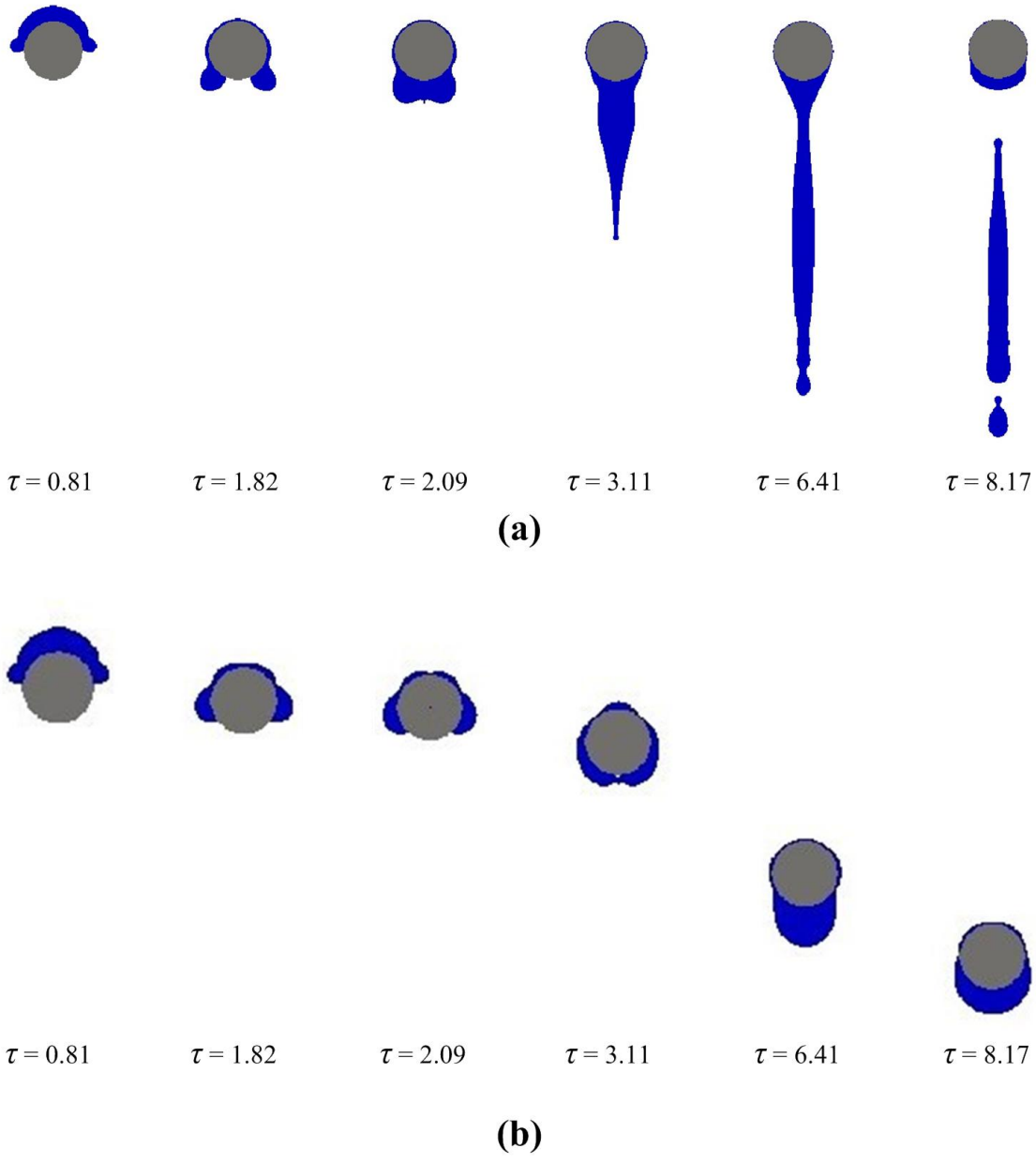

Fig. 10. Comparison of interface evolution between two collision systems (We = 50, Ω = 1, and θ_{eqi} = 20°). (a) collision with a stationary particle. (b) collision in mid-air.

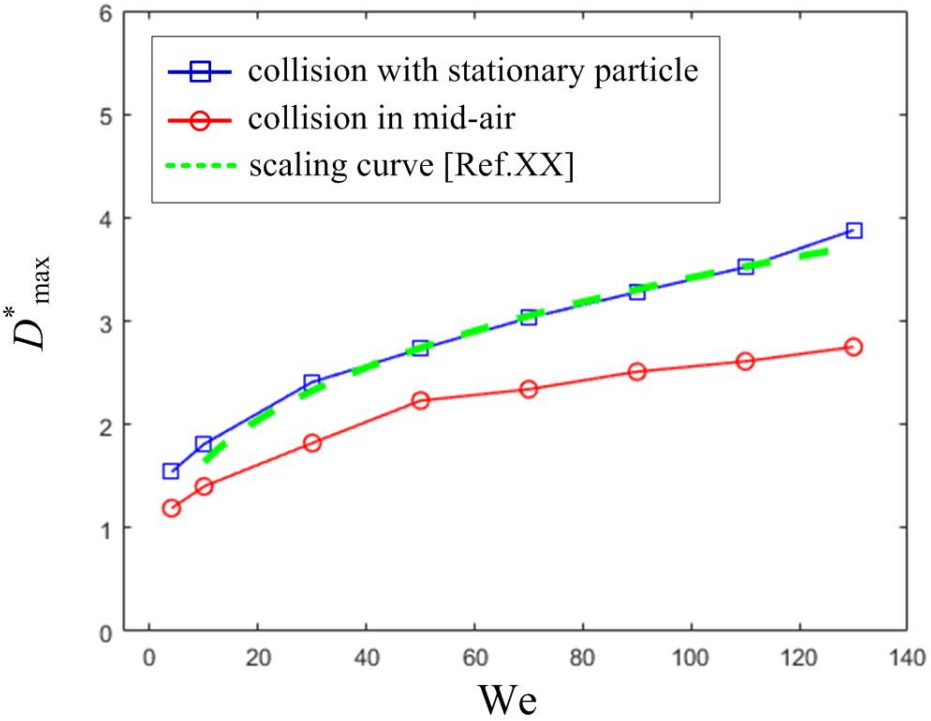

Fig. 11. Maximum spreading of droplet (D^*_{max}) as a function of Weber number ($4 \leq We \leq 130$). $\Omega = 0.5$ and $\theta_{eqi} = 90°$ for all cases. Green dashed line indicates the scaling result (i.e. $D^*_{max} \sim 0.9We^{0.32}\Omega^{0.2}$) for a collision with a stationary particle (Yoon and Shin, 2021c).

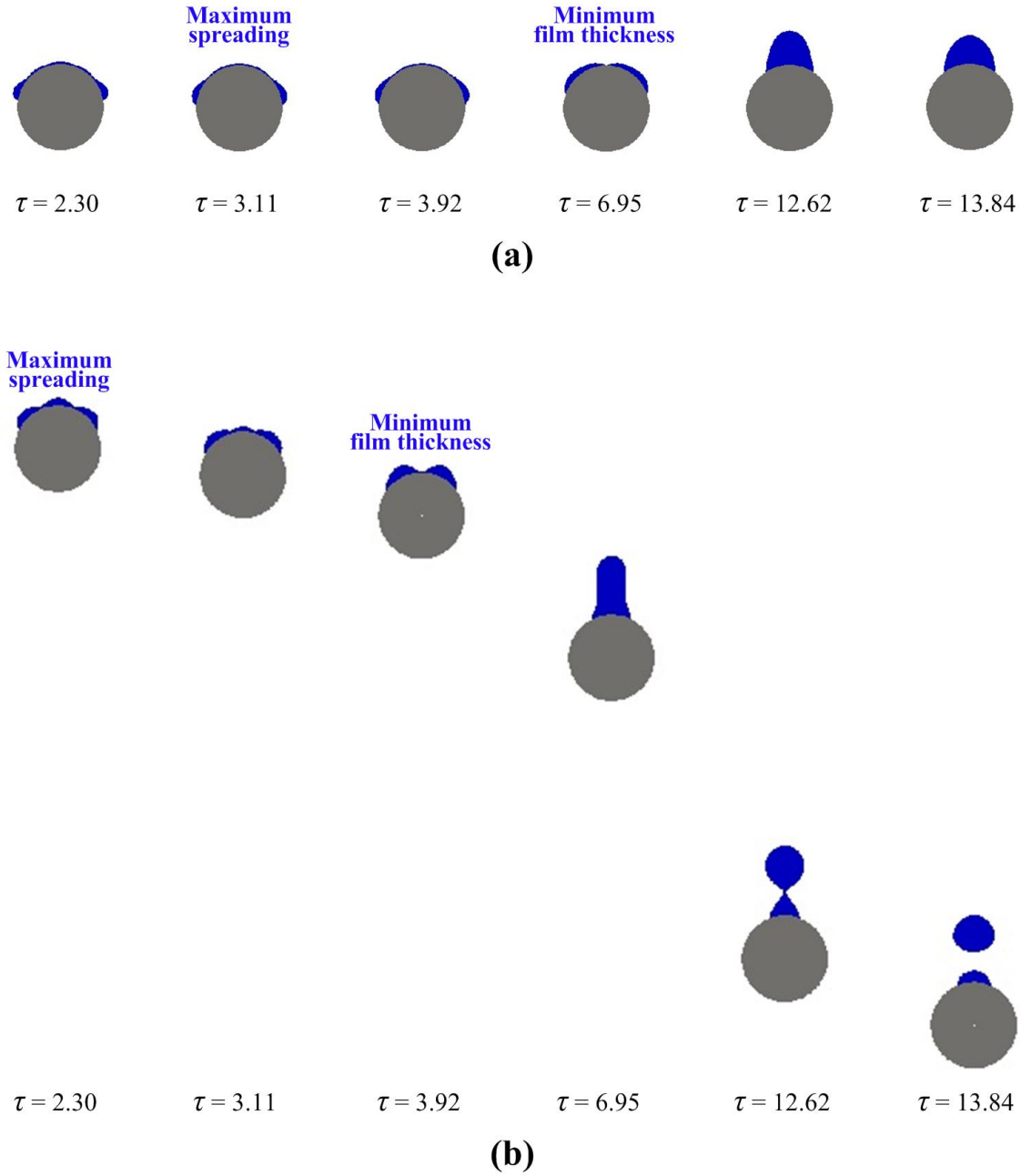

Fig. 12. Comparison of interface evolution between two collision systems (We = 50, Ω = 1/2, and θ_{eqi} = 20°). (a) collision with a stationary particle. (b) collision in mid-air.

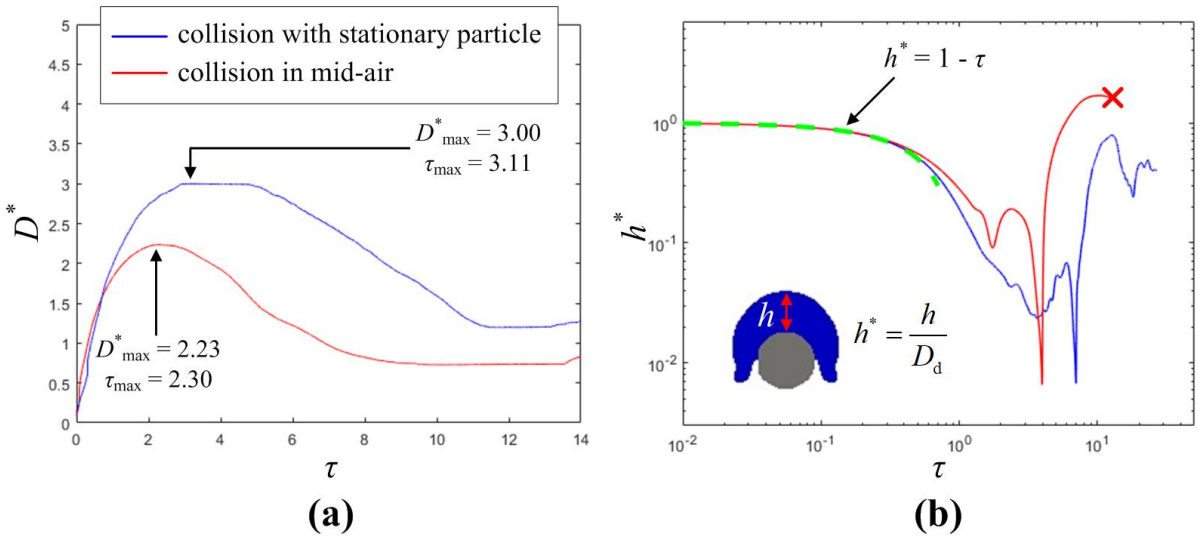

(a) **(b)**

Fig. 13. Dynamic profiles of the non-dimensional spreading diameter D^* and the non-dimensional film thickness h^* for two collision systems. (a) Non-dimensional spreading diameter (D^*). (b) Non-dimensional film thickness (h^*). Green dashed line indicates the universal trend ($h^* = 1 - \tau$).

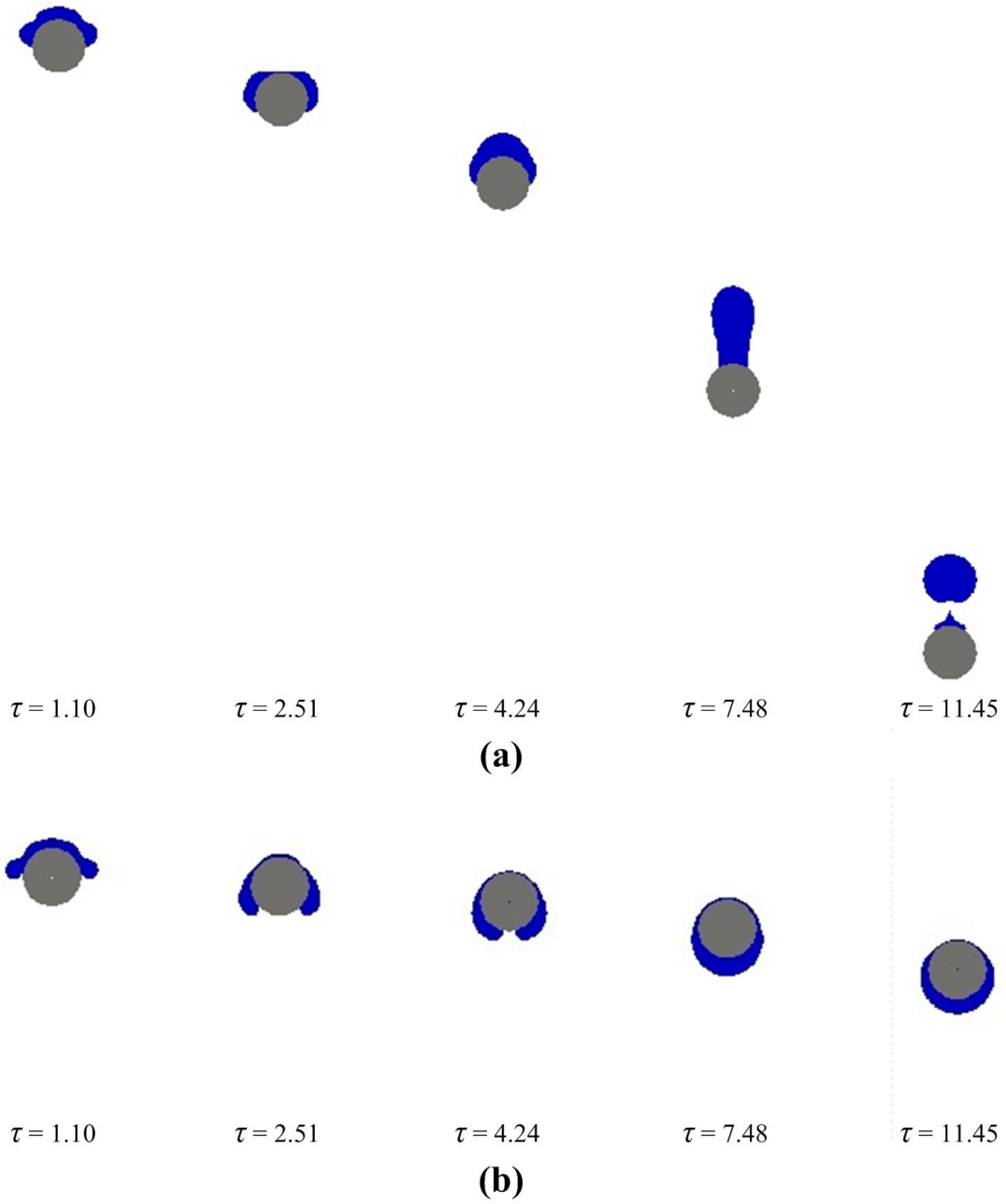

Fig. 14. Comparison of interface evolution between two collision cases in mid-air. (a) We = 30, Ω = 1, and θ_{eqi} = 20°. (b) We = 30, Ω = 1, and θ_{eqi} = 160°.

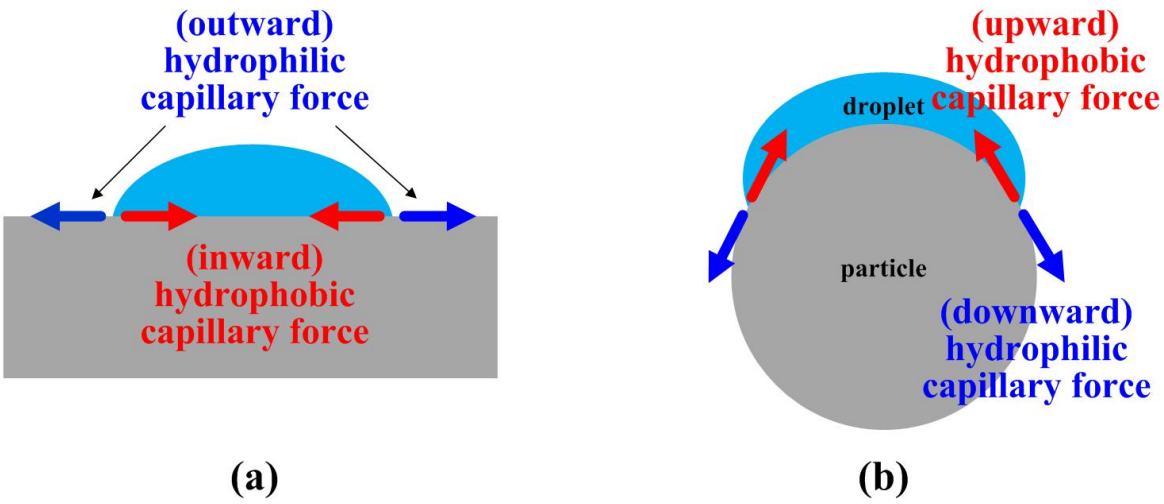

Fig. 15. Comparison of the direction of capillary forces acting in the vicinity of the contact line. (a) droplet collision with a flat surface. (b) droplet collision with a spherical particle.

TABLES

TABLE I. Comparison of computational time of the SDG AMR with the reference cases simulated using a uniform fine grid.

We	Grid type	Grid resolution	HRG layer re-grid parameter	HRG layer re-grid frequency (ξ)	Computational time (t_c, hour)	Normalized computational time (τ_c)
4	Uniform (reference)	CPR = 32	-	-	1.99	1
	SDG AMR	CPR_{HRG} = 32	$L_i = 0.10D_d$ $b_i = 0.01D_d$	0.777	0.26	0.13
67	Uniform (reference)	CPR = 32	-	-	8.63	1
	SDG AMR	CPR_{HRG} = 32	$L_i = 0.30D_d$ $b_i = 0.01D_d$	0.743	1.31	0.15
200	Uniform (reference)	CPR = 32	-	-	12.6	1
	SDG AMR	CPR_{HRG} = 32	$L_i = 0.50D_d$ $b_i = 0.01D_d$	0.717	1.76	0.14

References

Agresar, G., Linderman, J. J., Tryggvason, G. and Powell, K. G., "An Adaptive, Cartesian, Front-Tracking Method for the Motion, Deformation and Adhesion of Circulating Cells", J. Comput. Phys. 143 (2), 346-380 (1998).

Antonini, C., Amirfazli, A. and Marengo, M., "Drop impact and wettability: From hydrophilic to superhydrophobic surfaces," Phys. Fluids **24**, 102104 (2012).

Bakshi, S., Roisman, I. V. and Tropea, C., "Investigations on the impact of a drop onto a small spherical target," Phys. Fluids **19**, 032102 (2007).

Banitabaei, S. A. and Amirfazli, A., "Droplet impact onto a solid sphere: Effect of wettability and impact velocity," Phys. Fluids **29**, 062111 (2017).

Banitabaei, S. A. and Amirfazli, A., "Droplet impact onto a solid sphere in midair: Effect of viscosity, gas density, and diameter ratio on impact outcomes," Phys. Fluids **32**, 037102 (2020).

Bartolo, D., Josserand, C. and Bonn, D., "Retraction dynamics of aqueous drops upon impact on non-wetting surfaces", J. Fluid Mech. **545**, 329-338 (2005).

Berger, M. J. and Colella, P., "Local adaptive mesh refinement for shock hydrodynamics," J. Comput. Phys. 82, 64-84 (1989).

Bolleddula, D. A., Berchielli, A. and Aliseda, A., "Impact of a heterogeneous liquid droplet on a dry surface: Application to the pharmaceutical industry," Advances in Colloid and Interface Science, **159** (2) 144-159 (2010).

Ceniceros, H. D., Nós, R. L. and Roma, A. M., "Three-dimensional, fully adaptive simulations of phase-field fluid models", J. Comput. Phys. 229 (17), 6135-6155 (2010).

Ceniceros, H. D., Roma, A. M., Silveira-Neto, A. and Villar, M. M., "A Robust, Fully Adaptive Hybrid Level-Set/Front-Tracking Method for Two-Phase Flows with an Accurate Surface Tension Computation", Communications in Computational Physics 8, 1 (2010).

Choi, G. and Shin, S., "Numerical investigation of freely moving particle–droplet interaction with initial contact," JMST Adv. **1**, 57 (2019).

Chorin, A. J., "Numerical solution of the Navier-Stokes equations," Math. Comput. **22**, 745–762 (1968).

Clanet, C., Béguin, C., Richard, D. and Quéré, D., "Maximal deformation of an impacting drop," J. Fluid Mech. **517**, 199–208 (2004).

Dubrovsky, V.V., Podvysotsky, A.M. and Shraiber, A.A., "Particle interaction in three-phase polydisperse flows," Int. J. Multiph. Flow **18** (3), 337-352 (1992).

Fakhari, A. and Lee, T., "Finite-difference lattice Boltzmann method with a block-structured adaptive-mesh-refinement technique," Phys. Rev. E. 89, 033310 (2014).

Gac, J. M. and Gradon, L., “Lattice-Boltzmann modeling of collisions between droplets and particles,” Colloids Surf. A: Physicochem. Eng. Asp. **441**, 831–836 (2014).

Ge, Y. and Fan, L. “Droplet–particle collision mechanics with film-boiling evaporation,” J. Fluid Mech. **573**, 311-337 (2007).

Glowinski, R., Pan, T. W., Hesla, T. I. and Joseph, D. D., "A distributed Lagrange multiplier/fictitious domain method for particulate flows". Int. J. Multiph. Flow. 25, 755-794 (1999).

Griffith, B. E., Hornung, R. D., McQueen, D. M. and Peskin, C. S., "An adaptive, formally second order accurate version of the immersed boundary method," J. Comput. Phys. 223 (1), 10-49 (2007).

Han, J., Kim, W., Bae, C., Lee, D., Shin, S., Nam, Y. and Lee, C., "Contact time on curved superhydrophobic surfaces", Phys. Rev. E **101**, 043108 (2020)**.**

Hardalupas, Y., Taylor, A. M. K. P. and Wilkins, J. H., “Experimental investigation of sub-millimetre droplet impingement on to spherical surfaces,” Int. J. Heat Fluid Flow **20** (5), 477–485 (1999).

Harlow, F. H. and Welch, J. E., “Numerical calculation of time-dependent viscous incompressible flow of fluid with free surface,” Phys. Fluids **8**, 2182–2189 (1965).

He, P. Wang, D. and Zhu, C., " Liquid attachment and momentum transfer by collisions between free-fall solids and liquid spray droplets," Powder Technology **239**, 1-11 (2013).

Hoeven, M. J., “Particle-Droplet Collisions in Spray Drying (PhD Thesis)”, School of Engineering, The University of Queensland (2008).

Hoose, C., Lohmann, U., Bennartz, R., Croft, B. and Lesins, G., “Global simulations of aerosol processing in clouds,” Atmos. Chem. Phys. **8**, 6939–6963 (2008).

Josserand, C. and Thoroddsen, S. T., “Drop impact on a solid surface,” Ann. Rev. Fluid Mech. **48**, 365–391 (2016).

Khojasteh, D., Kazerooni, M., Salarian, S. and Kamali, R., “Droplet impact on superhydrophobic surfaces: A review of recent developments,” J. Indust. Eng. Chem. **42**, 1–14 (2016).

Khurana, G., Sahoo, N. and Dhar, P., "Phenomenology of droplet collision hydrodynamics on wetting and non-wetting spheres," Phys. Fluids **31**, 072003 (2019).

Liu, X., Zhang, X., and Min, J., "Maximum spreading of droplets impacting spherical surfaces", Phys. Fluids. **31**, 092102 (2019).

Malgarinos, I., Nikolopoulos, N. and Gavaises, M., “A numerical study on droplet-particle collision dynamics,” Int. J. Heat Fluid Flow **61**, 499–509 (2016).

Malgarinos, I., Nikolopoulos, N. and Gavaises, M., "Numerical investigation of heavy fuel droplet-particle collisions in the injection zone of a Fluid Catalytic Cracking reactor, Part I: Numerical model and 2D simulations,", Fuel Processing Technology **156**, 317-330 (2017).

Malgarinos, I., Nikolopoulos, N. and Gavaises, M., "Numerical investigation of heavy fuel droplet-particle collisions in the injection zone of a Fluid Catalytic Cracking reactor, part II: 3D simulations,", Fuel Processing Technology **156**, 43-53 (2017).

Mirzaii, I. and Passandideh-Fard, M., "Modeling free surface flows in presence of an arbitrary moving object," International Journal of Multiphase Flow 39, 216-226 (2012).

Mitra, S., Sathe, M. J., Doroodchi, E., Utikar, R., Shah, M. K., Pareek, V., Joshi, J. B. and Evans, G. M., "Droplet impact dynamics on a spherical particle," Chem. Eng. Sci. **100**, 105–119 (2013).

Mitra, S., Sathe, M. J., Dorrodchi, E., Pareek, V., Joshi, J. B. and Evans, G., "In-flight collision behaviour of droplets on a spherical particle falling under gravity," in NOVA (The University of Newcastle's Digital Repository, Australia (2013)

Mitra, S. Nguyen, T. B. T., Doroodchi, E., Pareek, V., Joshi, J. B. and Evans, G. M., "On wetting characteristics of droplet on a spherical particle in film boiling regime," Chem. Eng. Sci. **149**, 181-203 (2016)

Mitra, S., Evans, G. M., Doroodchi, E., Pareek, V. and Joshi, J. B., “Interactions in droplet and particle system of near unity size ratio,” Chem. Eng. Sci. **170**, 154–175 (2017).

Nedovic V., Kalusevic, A., Manojlovic, V., Levic, S. and Bugarski, B., "An overview of encapsulation technologies for food applications," Procedia Food Science **1**, 1806-1815 (2011).

Osher, S. and Sethian, J., “Fronts propagating with curvature-dependent speed: Algorithms based on Hamilton-Jacobi formulations,” J. Comput. Phys. **79**(1), 12–49 (1988).

Pasandideh-Fard, M., Chandra, S. and Mostaghimi, J., “A three-dimensional model of droplet impact and solidification,” Int. J. Heat Mass Transf. **45**(11), 2229–2242 (2002).

Pawar, S. K., Henrikson, F., Finotello, G., Padding, J. T., Deen, N. G., Jongsma, A., Innings, F. and Kuipers, J. H., “An experimental study of droplet-particle collisions,” Powder Technol. **300**, 157–163(2016).

Pivello, M. R., Villar, M. M., Serfaty, R., Roma, A. M. and Silveira-Neto, A., "A fully adaptive front tracking method for the simulation of two phase flows", Int. J. Multiph. Flow. 58, 72-82 (2014).

Popinet, S., "Gerris: a tree-based adaptive solver for the incompressible Euler equations in complex geometries," J. Comput. Phys. 190 (2), 572-600 (2003).

Rioboo, R., Marengo, M. and Tropea, C., “Time evolution of liquid drop impact onto solid, dry surfaces,” Exp. Fluids **33**, 112–124 (2002).

Roisman, I. V., Rioboo, R. and Tropea, C., “Normal impact of a liquid drop on a dry surface: model for spreading and receding,” Proc. R. Soc. Lond. A. **458**, 1411–1430 (2002).

Roma, A., Peskin, C. S. and Berger, M., "An Adaptive Version of the Immersed Boundary Method," J. Comput. Phys. 153 (2), 509-534 (1999).

Rozhkov, A., Prunet-Foch, B. and Vignes-Adler, M., “Impact of water drops on small targets,” Phys. Fluids **14**, 3485 (2002).

Rozhkov, A., Prunet-Foch, B. and Vignes-Adler, M., “Impact of drops of polymer solutions on small targets,” Phys. Fluids **15**, 2006 (2003).

Sechenyh, V. and Amirfazli, A., "An experimental study for impact of a drop onto a particle in mid-air: The influence of particle wettability," Journal of Fluids and Structures **66**, 282-292 (2016).

Shin, S. and Juric, D., “Modeling three-dimensional multiphase flow using a level contour reconstruction method for front tracking without connectivity,” J. Comput. Phys. **180**(2), 427–470 (2002).

Shin, S., Abdel-Khalik, S. I., Daru, V. and Juric, D., “Accurate representation of surface tension using level contour reconstruction method,” J. Comput. Phys. **203**(2), 493–516 (2005).

Shin, S. and Juric, D., "A hybrid interface method for three-dimensional multiphase flows based on front tracking and level set techniques", Int. J. Numer. Meth. Fluids **60,** 753-778 (2009).

Shin, S., Chergui, J. and Juric, D., "A solver for massively parallel direct numerical simulation of three-dimensional multiphase flows", Journal of Mechanical Science and Technology **31**(4), 1739-1751 (2017).

Shin, S., Chergui, J. and Juric, D., “Direct simulation of multiphase flows with modeling of dynamic interface contact,” Theor. Comput. Fluid Dyn. **32**(5), 655–687 (2018).

Shu, C. and Osher, S., "Efficient implementation of essentially non-oscillatory shock-capturing schemes, II", J. Comput. Phys. **83**(1) 32-78 (1989).

Šikalo, Š., Wilhelm, H.-D., Roisman, I. V., Jakirlić, S. and Tropea, C., “Dynamic contact angle of spreading droplets: Experiments and simulations,” Phys. Fluids **17**, 062103 (2005).

Sussman, M., Almgren, A. S., Bell, J. B., Colella, P., Howell, L. H. and Welcome, M. L., "An Adaptive Level Set Approach for Incompressible Two-Phase Flows", J. Comput. Phys. 148 (1), 81-124 (1999).

Teunou, E. and Poncelet, D., "Batch and continuous fluid bed coating – review and state of the art," Journal of Food Engineering, **53** (4), 325-340 (2002).

Tryggvason, G., Bunner, B., Esmaeeli, A., Juric, D., Al-Rawahi, N., Tauber, W., Han, J., Nas, S. and Jan, Y.J., "A front tracking method for the computations of multiphase flow," J. Comput. Phys. 169, 708–759 (2001).

Unverdi, S. and Tryggvason, G., "A front-tracking method for viscous, incompressible, multi-fluid flows," J. Comput. Phys. **100**, 25–37 (1992).

Usui, H., Nagara, A., Nunami, M. and Matsumoto, M., "Development of a Computational Framework for Block-based AMR Simulations", Procedia Computer Science 29, 2351-2359 (2014).

van der Holst, B. and Keppens, R., "Hybrid block-AMR in cartesian and curvilinear coordinates: MHD applications", J. Comput. Phys. 226 (1), 925-946 (2007).

Yang, B. and Chen, S., "Simulation of interaction between a freely moving solid particle and a freely moving liquid droplet by lattice Boltzmann method," Int. J. Heat Mass Transfer **127**, 474–484 (2018).

Yarin, A. L., "Drop Impact Dynamics: Splashing, Spreading, Receding, Bouncing, ...," Ann. Rev. Fluid Mech. **38**, 159 (2006).

Yokoi, K., Vadillo, D., Hinch, J. and Hutchings, I., “Numerical studies of the influence of the dynamic contact angle on a droplet impacting on a dry surface,” Phys. Fluids **21**, 072102 (2009).

Yoon, I. and Shin, S., " Computational study on dynamic behavior during droplet-particle interaction,” Chem. Eng. Sci. **241**, 116656 (2021).

Yoon, I. and Shin, S., "Direct numerical simulation of droplet collision with stationary spherical particle: A comprehensive map of outcomes", International Journal of Multiphase Flow **135**, 103503 (2021).

Yoon, I. and Shin, S., " Maximal spreading of droplet during collision on particle: effects of liquid viscosity and surface curvature,” Phys. Fluids **33**, 083310 (2021).

Zhang, Q., Qian, T. and Wang, X., “Phase field simulation of a droplet impacting a solid surface,” Phys. Fluids **28**, 022103 (2016).

Zhu, Y., Liu, H., Mu, K., Gao, P., Ding, H. and Lu, X., “Dynamics of drop impact onto a solid sphere: Spreading and retraction.” J. Fluid Mech. **824**, R3 (2017)

Zuzio, D. and Estivalezes, J. L., "An efficient block parallel AMR method for two phase interfacial flow simulations", Computers and Fluids 44 (1), 339-357 (2011).